

<sup>1</sup>  
<sup>2</sup> Susceptible host dynamics explain pathogen resilience to  
<sup>3</sup> perturbations

<sup>4</sup>

## <sup>5</sup> **Abstract**

<sup>6</sup> A major priority for epidemiological research in the time of anthropogenic change  
<sup>7</sup> is understanding how infectious disease dynamics respond to perturbations. Inter-  
<sup>8</sup> ventions to slow the spread of SARS-CoV-2 significantly disrupted the transmission  
<sup>9</sup> of other human pathogens. As interventions lifted, whether and when respiratory  
<sup>10</sup> pathogens would eventually return to their pre-pandemic dynamics remains to be  
<sup>11</sup> answered. Here, we present a framework for estimating pathogen resilience based  
<sup>12</sup> on how fast epidemic patterns approach their pre-pandemic, endemic dynamics and  
<sup>13</sup> analyze time series data from Hong Kong, Canada, Korea, and the US. By quanti-  
<sup>14</sup> fying the resilience of common respiratory pathogens, we are able to predict when  
<sup>15</sup> each pathogen will eventually return to pre-pandemic dynamics. Our predictions  
<sup>16</sup> closely match the observed deviations (or lack thereof) from its pre-COVID dynam-  
<sup>17</sup> ics. Discrepancies between predicted and observed dynamics indicate the long-term  
<sup>18</sup> impacts of pandemic perturbations, suggesting that some pathogens may be con-  
<sup>19</sup> verging to a different endemic cycle. Finally, we show that the replenishment rate  
<sup>20</sup> of the susceptible pool is a key determinant of pathogen resilience, which in turn  
<sup>21</sup> determines the sensitivity of a system to stochastic perturbations. Overall, our anal-  
<sup>22</sup> ysis highlights the persistent nature of common respiratory pathogens compared to  
<sup>23</sup> vaccine-preventable infections, such as measles.

## 24 Introduction

25 Non-pharmaceutical interventions to slow the spread of SARS-CoV-2 disrupted the  
 26 transmission of other human respiratory pathogens, adding uncertainties to their future  
 27 epidemic dynamics and their public health burden [1]. As interventions lifted,  
 28 large heterogeneities in outbreak dynamics were observed across different pathogens  
 29 in different countries, with some pathogens exhibiting earlier and faster resurgences  
 30 than others [2, 3, 4]. Heterogeneities in the overall reduction in transmission and the  
 31 timing of re-emergence likely reflect differences in intervention patterns, pathogen  
 32 characteristics, immigration/importation from other countries, and pre-pandemic  
 33 pathogen dynamics [5]. Therefore, comparing the differential impact of the pandemic  
 34 perturbations across pathogens can provide unique opportunities to learn  
 35 about underlying pathogen characteristics, such as their transmissibility or duration  
 36 of immunity, from heterogeneities in re-emergence patterns [6].

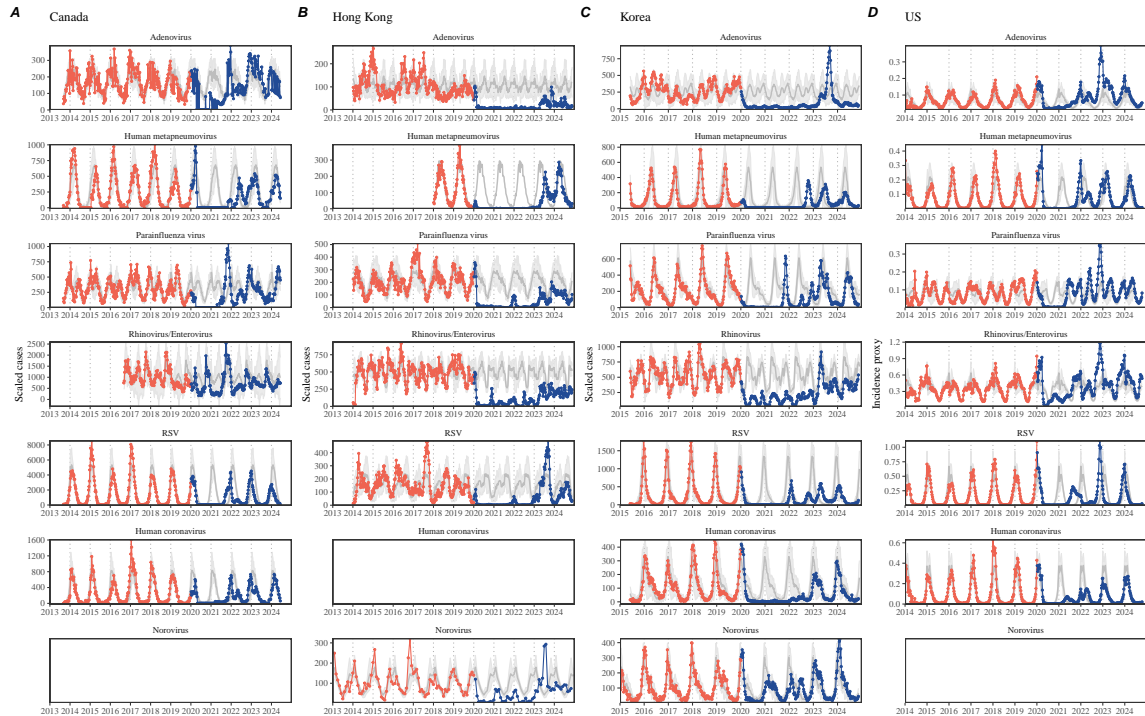


Figure 1: **Observed heterogeneity in responses to pandemic perturbations across respiratory pathogens and norovirus in (A) Canada, (B) Hong Kong, (C) Korea, and (D) US.** Red points and lines represent data before 2020. Blue points and lines represent data since 2020. Gray lines and shaded regions represent the mean seasonal patterns and corresponding 95% confidence intervals around the mean. Mean seasonal patterns were calculated by aggregating cases before 2020 into 52 weekly bins and taking the average in each week. Cases were scaled to account for changes in testing patterns (Materials and Methods).

37 Even though more than five years have passed since the emergence of SARS-CoV-  
38 2, we still observe persistent changes in pathogen dynamics following the pandemic  
39 perturbations. For example, compared to pre-pandemic, seasonal patterns, human  
40 metapneumovirus in Korea seems to circulate at lower levels, whereas RSV in Korea  
41 seems to exhibit different seasonality (Figure 1). These observations suggest a fun-  
42 damental change in pathogen dynamics following the pandemic perturbations, which  
43 might be driven by a long-term shift in either human behavior or population-level  
44 immunity [7, 8]. For example, the emergence of SARS-CoV-2 could have caused  
45 a long-term shift in population-level immunity through its interactions with other  
46 pathogens [9], especially with seasonal coronaviruses [7, 10, 11]. The possibility of a  
47 long-lasting impact of the pandemic perturbations poses an important question for  
48 future infectious disease dynamics: can we predict whether and when other pathogens  
49 will eventually return to their pre-pandemic dynamics?

50 So far, most analyses of respiratory pathogens after pandemic perturbations have  
51 focused on characterizing the timing of rebound [1, 12, 5]. Instead, we seek to char-  
52 acterize how fast (and whether) a pathogen returns to its pre-pandemic dynamics.  
53 These two concepts have a subtle but important difference. For example, it took  
54 more than 3 years for human metapneumovirus to rebound in Hong Kong, but the  
55 observed epidemic patterns in 2024 appear similar to pre-pandemic seasonal means,  
56 suggesting a possible return to pre-pandemic dynamics, though confirmation may  
57 require multiple seasons (Figure 1). Measuring this rate of return is useful because it  
58 allows us to quantify the ecological resilience of a host-pathogen system, which can  
59 inform responses to future interventions [13, 14, 15, 16].

60 In this study, we lay out theoretical and statistical approaches to characterizing  
61 the resilience of a host-pathogen system based on how fast the system recovers from  
62 perturbation. We begin by laying out a few representative scenarios that capture  
63 the potential impact of pandemic perturbations on endemic pathogen dynamics and  
64 illustrate how resilience can be measured by comparing the pre- and post-pandemic  
65 dynamics of susceptible and infected hosts. In practice, information on suscepti-  
66 ble hosts is often unavailable, making this theoretical approach infeasible. Instead,  
67 we utilize a mathematical technique to reconstruct empirical attractors from the  
68 data [17], which allows us to measure the rate at which the host-pathogen system  
69 approaches this empirical attractor after a perturbation; we define this rate to be  
70 the empirical resilience of the host-pathogen system. We use this method to ana-  
71 lyze pathogen surveillance data for respiratory and non-respiratory pathogens from  
72 Canada, Hong Kong, Korea, and the US. Finally, we show that susceptible host dy-  
73 namics explain variation in pathogen resilience and further demonstrate that more  
74 resilient pathogens will be less sensitive to perturbations caused by demographic  
75 stochasticity, thereby providing a direct link between pathogen resilience and persis-  
76 tence.

## <sup>77</sup> Conceptual introduction to pathogen resilience

<sup>78</sup> In classical ecological literature, the resilience of an ecological system is measured by  
<sup>79</sup> the rate at which the system returns to its reference state following a perturbation  
<sup>80</sup> [13, 14, 15, 16]. This rate corresponds to the largest real part of the eigenvalues  
<sup>81</sup> of the linearized system near equilibrium—here, we refer to this value as the *in-*  
<sup>82</sup> *trinsic* resilience of the system, which represents the expected rate of return from  
<sup>83</sup> perturbed states. In practice, we rarely know the true model describing population-  
<sup>84</sup> level dynamics of common respiratory pathogens, limiting our ability to infer the  
<sup>85</sup> intrinsic resilience of a system. Instead, we can measure the *empirical* resilience  
<sup>86</sup> of a host-pathogen system by looking at how fast the system returns to the pre-  
<sup>87</sup> perturbation, endemic dynamics after the perturbation has ended. The COVID-19  
<sup>88</sup> pandemic provides a particularly useful example of a major perturbation, providing  
<sup>89</sup> unique opportunities to measure the resilience of a host-pathogen system.

<sup>90</sup> As an example, we begin with a simple Susceptible-Infected-Recovered-Susceptible  
<sup>91</sup> (SIRS) model with seasonally forced transmission and demography (i.e., birth and  
<sup>92</sup> death). The SIRS model is the simplest model that allows for the waning of im-  
<sup>93</sup> munity and is commonly used for modeling the dynamics of respiratory pathogens  
<sup>94</sup> [18]. First, consider a pandemic perturbation that reduces transmission by 50% for 6  
<sup>95</sup> months starting in 2020, which causes epidemic patterns to deviate from their origi-  
<sup>96</sup> nal stable annual cycle for a short period of time and eventually come back (Figure  
<sup>97</sup> 2A). To measure the resilience of this system empirically, we first need to be able to  
<sup>98</sup> measure the distance from its pre-pandemic attractor, which is defined as a set of  
<sup>99</sup> points in state space or phase plane that the system is pulled towards [19]. There  
<sup>100</sup> are many ways we can measure the distance from the attractor, but for illustrative  
<sup>101</sup> purposes, we choose one of the most parsimonious approaches: that is, we look at  
<sup>102</sup> how the susceptible (S) and infected (I) populations change over time and measure  
<sup>103</sup> the Euclidean distance on the SI phase plane, using the counterfactual unperturbed  
<sup>104</sup> phase plane as a reference (Figure 2B; Materials and Methods). In this simple case,  
<sup>105</sup> the locally estimated scatterplot smoothing (LOESS) fit indicates that the distance  
<sup>106</sup> from the attractor decreases exponentially (linearly on a log scale) on average (Figure  
<sup>107</sup> 2C). Furthermore, the overall rate of return approximates the intrinsic resilience of  
<sup>108</sup> the seasonally unforced system (Figure 2C).

<sup>109</sup> Alternatively, pandemic perturbations can have a lasting impact on the forces  
<sup>110</sup> driving pathogen dynamics through a long-term reduction in transmission or per-  
<sup>111</sup> manent change in immunity. As an example, we consider a scenario in which a 10%  
<sup>112</sup> reduction in transmission persists even after the major pandemic perturbations are  
<sup>113</sup> lifted (Figure 2D–F). In such cases, we cannot know whether the pathogen will re-  
<sup>114</sup> turn to its original cycle or a different cycle until many years have passed, and we  
<sup>115</sup> cannot measure the distance to the new unknown attractor that the system might  
<sup>116</sup> eventually approach. Nonetheless, we can still measure the distance from the pre-  
<sup>117</sup> pandemic attractor and ask how the distance changes over time (Figure 2E). The  
<sup>118</sup> LOESS fit suggests that the distance from the pre-pandemic attractor will initially

119 decrease exponentially on average (equivalently, linearly on a log scale) and even-  
120 tually plateau (Figure 2F). Here, a permanent 10% reduction in transmission rate  
121 slows the system, which causes the distance from the pre-pandemic attractor initially  
122 to decrease at a slower rate (Figure 2F) than it would have otherwise (Figure 2C)  
123 before plateauing at a fixed distance between the two attractors. This example shows  
124 that resilience is not necessarily an intrinsic property of a specific pathogen. Instead,  
125 pathogen resilience is a property of a specific attractor that a host-pathogen system  
126 approaches, which depends on both pathogen and host characteristics.

127 Finally, transient phenomena can further complicate the picture (Figure 2G–I).  
128 For example, a stage-structured model, which accounts for reduction in secondary  
129 susceptibility, initially exhibits a stable annual cycle, but perturbations from a 10%  
130 reduction in transmission for 6 months cause the epidemic to shift to biennial cycles  
131 (Figure 2G). The system eventually approaches the original pre-pandemic attractor  
132 (Figure 2H), suggesting that this biennial cycle is a transient phenomenon. The  
133 LOESS fit indicates that the distance from the attractor initially decreases expo-  
134 nentially at a rate that is consistent with the intrinsic resilience of the seasonally  
135 unforced stage-structured system, but the approach to the attractor slows down  
136 with the damped oscillations (Figure 2I). This behavior is also referred to as a ghost  
137 attractor, which causes long transient dynamics and slow transitions [20]. Strong  
138 seasonal forcing in transmission can also lead to transient phenomena for a simple  
139 SIRS model, causing a slow return to pre-perturbation dynamics (Supplementary  
140 Figure S1).

141 This empirical approach allows us to measure the resilience of a two-strain host-  
142 pathogen system as well even when we have incomplete observation of the infection  
143 dynamics. Simulations from a simple two-strain competition system illustrate that  
144 separate analyses of individual strain dynamics (e.g., RSV A vs B) and a joint anal-  
145 ysis of total infections (e.g., total RSV infections) yield identical resilience estimates  
146 (Supplementary Figure S2, 3). This is expected because eigenvalues determine the  
147 dynamics of the entire system around the equilibrium, meaning that both strains  
148 should exhibit identical rates of return following a perturbation. Analogous to a  
149 single-strain system, strong seasonal forcing in transmission can cause the two-strain  
150 system to slow down through transient phenomena (Supplementary Figure S4).

151 These observations yield three insights. First, we can directly estimate the empircal  
152 resilience of a host-pathogen system by measuring the rate at which the system  
153 approaches an attractor, provided that we have a way to quantify the distance from  
154 the attractor—as we discuss later, the attractor of a system can be reconstructed  
155 from data from mathematical theory without making assumptions about the under-  
156 lying model. The empirical approach to estimating pathogen resilience is particularly  
157 convenient because it does not require us to know the true underlying model; esti-  
158 mating the intrinsic resilience from fitting misspecified models can lead to biased  
159 estimates (Supplementary Figure S5). Second, resilience estimates allow us to make  
160 phenomenological predictions about the dynamics of a host-pathogen system follow-  
161 ing a perturbation. Assuming that an attractor has not changed and the distance

from the attractor will decrease exponentially over time, we can estimate when the system should reach an attractor. Finally, a change in the (exponential) rate of approach provide information about whether the system has reached an alternative attractor, or a ghost attractor, that is different from the original, pre-pandemic attractor. These alternative attractors may reflect permanent changes in transmission patterns as well as changes in immune landscapes. There will be periods of time when it is difficult to tell whether pathogen dynamics are still diverging from the original attractor due to a long-term perturbation, or have entered the basin of attraction of a new attractor. Now that several years have passed since major interventions have been lifted, many respiratory pathogens may have had sufficient time to begin returning to their post-intervention attractors—empirical comparisons between current cases and pre-pandemic cases are consistent with this hypothesis (Figure 1). With recent data, we can start to evaluate whether we see early signs of convergence to the former attractor or a new one.

## Inferring pathogen resilience from real data

Based on these observations, we now lay out our approach to estimating pathogen resilience from real data (Figure 3). We first tested this approach against simulations and applied it to real data. Specifically, we analyzed case time series of respiratory pathogens from four countries: Canada, Hong Kong, Korea, and the US.

So far, we have focused on simple examples that assume a constant transmission reduction during the pandemic. However, in practice, the impact of pandemic perturbations on pathogen transmission was likely more complex (Figure 3A), reflecting introduction and relaxation of various intervention strategies. In some cases, strong perturbations likely caused local fadeouts, requiring immigration/importation from another location for epidemic rebound. Such complexities could lead to longer delays between the introduction of pandemic perturbations and pathogen rebound as well as temporal variation in outbreak sizes (Figure 3B); in this example, continued transmission reduction from interventions limits the size of the first outbreak in 2021 following the rebound, allowing for a larger outbreak in 2022 when interventions are further relaxed.

Previously, we relied on the dynamics of susceptible and infected hosts to compute the distance from the attractor (Figure 2), but information on susceptible hosts is rarely available in practice. In addition, uncertainties in case counts due to observation error, strain evolution, and multiannual cycles in the observed epidemic dynamics (e.g., adenovirus circulation patterns in Hong Kong and Korea) add challenges to defining pre-pandemic attractors, which limits our ability to measure the distance from the attractor. To address these challenges, we can reconstruct an empirical attractor by utilizing Takens' theorem [17], which states that an attractor of a nonlinear multidimensional system can be mapped onto a delayed embedding (Materials and Methods). For example, we can use delayed logged values of pre-pandemic

202 cases  $C(t)$  (Figure 3C) to reconstruct the attractor:

$$\langle \log(C(t) + 1), \log(C(t - \tau) + 1), \dots, \log(C(t - (M - 1)\tau) + 1) \rangle, \quad (1)$$

203 where the delay  $\tau$  and embedding dimension  $M$  are determined based on autocor-  
204 relations and false nearest neighbors, respectively [21, 22]. This allows us to define  
205 the pre-pandemic attractor as a points on an  $M$  dimensional space. We can then  
206 apply the same delay and embedding dimensions to the entire time series to deter-  
207 mine the position in multi-dimensional state space (Figure 3D), which allows us to  
208 measure the nearest neighbor distance between the current state of the system and  
209 the empirical pre-pandemic attractor (Figure 3E). Specifically, the nearest neighbor  
210 distance is calculated by computing the distance between the current position on  
211 the  $M$  dimensional space and all points in the empirical attractor set and taking the  
212 minimum value. In theory, we can now quantify how fast this distance decreases by  
213 fitting a linear regression on a log scale, where the slope of the linear regression em-  
214 pirically measures pathogen resilience with a steeper slope corresponding to a higher  
215 resilience estimate (Figure 3E). However, resulting estimates of pathogen resilience  
216 can be sensitive to choices about embedding delays and dimensions. For example,  
217 using longer delays and higher dimensions tends to smooth out temporal variations  
218 in the distance from the attractor (Supplementary Figure S6).

219 Complex changes in the distance from the attractor suggest that estimating  
220 pathogen resilience from linear regression will be particularly sensitive to our choice  
221 of fitting windows for the regression (Figure 3E). Therefore, before we tried estimat-  
222 ing resilience from real data, we explored an automated window selection criterion  
223 for linear regression and tested it against randomized, stochastic simulations across  
224 a range of realistic pandemic perturbation shapes. In doing so, we also explored  
225 optimal choices for embedding dimensions and evaluated our choices of fitting win-  
226 dow parameters and embedding dimensions by quantifying correlation coefficients  
227 between the estimated resilience and the intrinsic resilience of a seasonally unforced  
228 system (Materials and Methods). Overall, we found large variation in estimation  
229 performances with correlation coefficient ranging from 0.21 to 0.61 (Supplementary  
230 Figure S7). In almost all cases, the automated window selection approach outper-  
231 formed a naive approach, which performs regression between the peak distance and  
232 current distance (Supplementary Figure S7).

233 Based on the best performing window selection criteria and embedding dimen-  
234 sion, we applied this approach to pathogen surveillance data presented in Figure  
235 1 (Materials and Methods). For each time series, we applied Takens' theorem in-  
236 dependently to reconstruct the empirical attractor and obtained the corresponding  
237 time series of distances from attractors (Supplementary Figure S8). Then, we used  
238 the automated window selection criterion to fit a linear regression and estimated the  
239 empirical resilience for each pathogen in each country (Supplementary Figure S8);  
240 the window selection criterion gave poor regression window for three cases (norovirus  
241 in Hong Kong and Korea and rhinovirus/enterovirus in the US), leading to unreal-  
242 istically low resilience estimates, and so we used ad-hoc regression windows instead

243 (Supplementary Figure S9; Materials and Methods).

244 For all pathogens we considered, resilience estimates fell between 0.4/year and  
245 1.8/year (Figure 4A). We estimated the mean resilience of common respiratory  
246 pathogens to be 0.99/year (95% CI: 0.81/year–1.18/year). For reference, this is  
247  $\approx$  7.5 times higher than the intrinsic resilience of pre-vaccination measles in England  
248 and Wales ( $\approx$  0.13/year). Finally, resilience estimates for norovirus, a gastrointesti-  
249 nal pathogen, were comparable to those of common respiratory pathogens: 1.44/year  
250 (95% CI: 1.01/year–1.87/year) for Hong Kong and 1.07/year (95% CI: 0.86/year–  
251 1.29/year) for Korea. Based on a simple ANOVA test, we did not find significant  
252 differences in resilience estimates across countries ( $p = 0.25$ ) or pathogens ( $p = 0.67$ ).

253 Using resilience estimates, we predicted when each pathogen would hypothetically  
254 return to their pre-pandemic dynamics, assuming no long-term change in the attrac-  
255 tor. Specifically, we extended our linear regression fits to distance-from-attractor  
256 time series and ask when the predicted regression line will cross a threshold value;  
257 since we relied on nearest neighbor distances, pre-pandemic distances are always  
258 greater than zero (Figure 3E), meaning that we can use the mean of pre-pandemic  
259 distances as our threshold.

260 We predicted that a return to pre-pandemic cycles has occurred or would be  
261 imminent for most pathogens (Figure 4B). In particular, we predicted that 12 out  
262 of 23 pathogen-country pairs should have already returned before the end of 2024.  
263 For almost all pathogens that were predicted to have returned already, the observed  
264 epidemic dynamics showed clear convergence towards their pre-pandemic seasonal  
265 averages, confirming our predictions (Figure 4C). However, there were a few ex-  
266 ceptions, including norovirus in Hong Kong and rhinovirus/enterovirus in the US,  
267 where the observed epidemic dynamics in 2024 exhibit clear deviation from their pre-  
268 pandemic seasonal averages (Figure 4C; Figure S9). These observations suggest a  
269 possibility that some common respiratory pathogens may have converged to different  
270 attractors or are still exhibiting non-equilibrium dynamics. In contrast, pathogens  
271 that were predicted to have not returned yet also showed clear differences from their  
272 pre-pandemic seasonal averages; as many of these pathogens are predicted to return  
273 in 2025–2026, we may be able to test these predictions in near future (Supplementary  
274 Figure S10). Our reconstructions of distance time series and estimates of pathogen  
275 resilience and expected return time were generally robust to choices of embedding  
276 dimensions (Supplementary Figure S11–12).

## 277 Susceptible host dynamics explain variation in pathogen 278 resilience

279 So far, we have focused on quantifying pathogen resilience from the observed pat-  
280 terns of pathogen re-emergence following pandemic perturbations. But what factors  
281 determine how resilient a host-pathogen system is? To address this question, we used  
282 the SIRS model to explore how changes in susceptible host dynamics affect pathogen

resilience. To do so, we varied the basic reproduction number  $\mathcal{R}_0$ , which represents the average number of secondary infections caused by a newly infected individual in a fully susceptible population, and the duration of immunity and computed intrinsic resilience for each parameter.

We found that an increase in  $\mathcal{R}_0$  and a decrease in the duration of immunity correspond to an increase in pathogen resilience (Figure 5A). Similarly, an increase in  $\mathcal{R}_0$  and a decrease in the duration of immunity corresponds to a faster per-capita rate of susceptible replenishment, which is defined as the ratio between absolute rate at which new susceptibles enter the population and the equilibrium number of susceptible individuals in the population,  $S^*$  (Figure 5B). We note that a higher  $\mathcal{R}_0$  drives a faster per-capita susceptible replenishment rate by decreasing the susceptible proportion at equilibrium,  $S^*$ . For a simple SIR model that assumes a life-long immunity, we can show analytically that pathogen resilience is proportional to the per-capita rate of susceptible replenishment (Materials and Methods). Overall, these observations suggest that a faster per-capita susceptible replenishment rate causes the system to be more resilient.

By taking the average values of empirical resilience values for each pathogen, we were able to map each pathogen onto a set of parameters of the SIRS model that are consistent with corresponding resilience estimates (Figure 5A). Across all pathogens we considered, we estimated that the average duration of immunity is likely to be short ( $< 4$  years) across a plausible range of  $\mathcal{R}_0$  ( $< 6$ ). We were also able to obtain a plausible range of susceptible replenishment rates for each pathogen (Figure 5B), but there was a large uncertainty in the estimates for susceptible replenishment rates due to a lack of one-to-one correspondence between susceptible replenishment rates and pathogen resilience.

## Pathogen resilience determines sensitivity to stochastic perturbations

Even in the absence of major pandemic perturbations, host-pathogen systems are expected to experience continued perturbations of varying degrees from changes in epidemiological conditions, such as human behavior, climate, and viral evolution. These perturbations can also arise from demographic stochasticity, which is inherent to any ecological systems. Here, we used a seasonally unforced SIRS model with birth/death to explore how resilience of a host-pathogen system determines the sensitivity to perturbations caused by demographic stochasticity (Materials and Methods).

We found that resilience of a host-pathogen system determines the amount of deviation from the deterministic trajectory caused by demographic stochasticity, with less resilient systems experiencing larger deviations (Figure 6). Notably, less resilient systems also exhibited slower epidemic cycles (Figure 6A–C). The periodicity of this epidemic cycle matched those predicted by the intrinsic periodicity of the system

323 (Supplementary Figure S13) where the intrinsic resilience of the system is inversely  
324 proportional to its intrinsic periodicity (Supplementary Figure S14). However, we  
325 note that the interplay between seasonal transmission and intrinsic periodicity can  
326 also lead to complex cycles, as illustrated by a recent analysis of *Mycoplasma pneumoniae*  
327 dynamics [23].

328 We also note that the intrinsic resilience is not the sole determinant for how sen-  
329 sitive the system is to stochastic perturbations. For example, the population size  
330 and average duration of infection also affect the amount of deviation from the deter-  
331 ministic trajectory caused by demographic stochasticity, even though these quantities  
332 have little to no impact on the intrinsic resilience (Supplementary Figure S15). These  
333 conclusions were robust for the seasonally forced SIRS model (Supplementary Figure  
334 S16).

## 335 Discussion

336 COVID-19 pandemic interventions caused major disruptions to circulation patterns  
337 of both respiratory and non-respiratory pathogens, adding challenges to predicting  
338 their future dynamics [1, 2, 3, 4]. However, these perturbations offer large-scale natu-  
339 ral experiments for understanding how different pathogens respond to perturbations.  
340 In this study, we showed that pathogen re-emergence patterns following pandemic  
341 perturbations can be characterized through the lens of ecological resilience and pre-  
342 sented a new method for estimating pathogen resilience from time series data. We  
343 showed that variation in pathogen resilience can be explained by the differences in  
344 susceptible host dynamics, where faster replenishment of the susceptible pool corre-  
345 sponds to a more resilient host-pathogen system. Finally, we showed that pathogen  
346 resilience also determines the sensitivity to stochastic perturbations.

347 We analyzed case time series of common respiratory infections and norovirus  
348 infections from Canada, Hong Kong, Korea, and the US to estimate their resilience.  
349 Overall, we estimated the resilience of these pathogens to range from 0.4/year to  
350 1.8/year, which is 3–14 times more resilient than prevaccination measles. Consistent  
351 with other epidemiological evidence [24, 25, 26, 27], these resilience estimates indicate  
352 that common respiratory pathogens and norovirus likely exhibit faster susceptible  
353 replenishment and are therefore more persistent, indicating potential challenges in  
354 controlling these pathogens.

355 Based on our resilience estimates, we made phenomenological predictions about  
356 when each pathogen will return to their endemic cycles. For the most part, we  
357 accurately predicted which pathogens should have already returned before the end  
358 of 2024. However, there were two main exceptions (i.e., norovirus in Hong Kong  
359 and rhinovirus/enterovirus in the US), suggesting that these pathogens may be con-  
360 verging to new endemic cycles or experiencing long-term transient behavior. These  
361 changes may reflect changes in surveillance or actual shift in the dynamics, caused  
362 by permanent changes in behavior or population-level immunity. While it may seem

363 unlikely that permanent changes in behavior would only affect a few pathogens and  
364 not others, we cannot rule out this possibility given differences in the observed mean  
365 age of infections and therefore the differences in age groups that primarily drive  
366 transmission [28, 29]. Differences in the mode of transmission between respiratory  
367 vs gastrointestinal pathogens may also contribute to the differences in responses to  
368 pandemic perturbations.

369 For almost half of the pathogens we considered, we predicted that their return  
370 to original epidemic patterns is imminent. We will need a few more years of data  
371 to test whether these pathogens will eventually return to their original dynamics or  
372 eventually converge to a different attractor. We also cannot rule out the possibility  
373 that some pathogens may exhibit long-term transient behaviors following pandemic  
374 perturbations. Overall, these observations echo earlier studies that highlighted the  
375 long-lasting impact of pandemic perturbations [8, 30, 31, 4, 23].

376 We showed that susceptible host dynamics shape pathogen resilience, where faster  
377 replenishment of the susceptible population causes the pathogen to be more resilient.  
378 For simplicity, we focused on waning immunity and birth as the main drivers of the  
379 susceptible host dynamics but other mechanisms can also contribute to the replenish-  
380 ment of the susceptible population. In particular, pathogen evolution, especially the  
381 emergence of antigenically novel strains, can cause effective waning of immunity in  
382 the population; therefore, we hypothesize that the rate of antigenic evolution is likely  
383 a key feature of pathogen resilience. Future studies should explore the relationship  
384 between the rate of evolution and resilience for antigenically evolving pathogens.

385 Quantifying pathogen resilience also offers novel approaches to validating population-  
386 level epidemiological models. So far, most model validation in infectious disease ecol-  
387 ogy is based on the ability of a model to reproduce the observed epidemic dynamics  
388 and to predict future dynamics [32, 33, 26, 34, 35]. However, many models can  
389 perform similarly under these criteria. For example, two major RSV models have  
390 been proposed to explain biennial epidemic patterns: (1) a stage- and age-structured  
391 model that allows disease severity to vary with number of past infections and age of  
392 infection [26] and (2) a pathogen-interaction model that accounts for cross immunity  
393 between RSV and human metapneumovirus [33]. Since both models can accurately  
394 reproduce the observed epidemic patterns, standard criteria for model validation  
395 do not allow us to distinguish between these two models from population-level data  
396 alone. Instead, it would be possible to measure the empirical resilience of each model  
397 by simulating various perturbations and comparing the simulations to estimates of  
398 empirical resilience from data, using pandemic perturbations as a reference.

399 There are several limitations to our work. First, we did not extensively explore  
400 other approaches to reconstructing the attractor. Recent studies showed that more  
401 sophisticated approaches, such as using non-uniform embedding, can provide more  
402 robust reconstruction for noisy data [22]. In the context of causal inference, choices  
403 about embedding can have major impact on the resulting inference [36]. Our re-  
404 silience estimates are likely overly confident given a lack of uncertainties in attractor  
405 reconstruction as well as the simplicity of our statistical framework. Nonetheless,

as illustrated in our sensitivity analyses, inferences about pathogen resilience in our SIRS model appear to be robust to decisions about embedding lags and dimensions—this is because tracking the rate at which the system approaches the attractor is likely a much simpler problem than making inferences about causal directionality. Short pre-pandemic time series also limit our ability to accurately reconstruct the attractor and contribute to the crudeness of our resilience estimates; although this is less likely a problem for respiratory pathogens that are strongly annual, our attractor reconstruction may be inaccurate for those exhibiting multi-annual cycles, such as adenovirus in Hong Kong and Korea. Our framework also do not allow us to distinguish whether a system has settled to a new attractor or is experiencing long-term transient behavior. Uncertainties in pathogen dynamics due to changes in testing patterns further contribute to the crudeness of our resilience estimates. Despite these limitations, our qualitative prediction that common respiratory pathogens are more resilient than prevaccination measles is also likely to be robust, given how rapidly many respiratory pathogens returned to their original cycles following pandemic perturbations.

Predicting the impact of anthropogenic changes on infectious disease dynamics is a fundamental aim of infectious disease research in a rapidly changing world. Our study illustrates that how a host-pathogen system responds to both small and large perturbations is largely predictable through the lens of ecological resilience. In particular, quantifying the resilience of a host-pathogen system offers a unique insight into questions about endemic pathogens' responses to pandemic perturbations, including whether some pathogens will exhibit long-lasting impact from the pandemic perturbation or not. More broadly, a detailed understanding of the determinants of pathogen resilience can provide deeper understanding of pathogen persistence.

## Materials and Methods

### Data

We gathered time series on respiratory infections from Canada, Hong Kong, Korea, and United States (US). As a reference, we also included time series data on norovirus infections when available. In contrast to respiratory pathogens, we hypothesized gastrointestinal viruses, such as norovirus, to be differently affected by pandemic perturbations.

Weekly time series of respiratory infection cases in Canada came from a publicly available website by the Respiratory Virus Detection Surveillance System, which collects data from select laboratories across Canada [37]. Weekly time series of respiratory infection cases in Hong Kong came from a publicly available website by the Centre for Health Protection, Department of Health [38, 39]. Weekly time series of acute respiratory infection cases in Korea came from a publicly available website by the Korea Disease Control and Prevention Agency [40]. Finally, weekly time series of respiratory infection cases in the US were obtained from the National Respiratory

446 and Enteric Virus Surveillance System. Time series on number of tests were also  
447 available in Canada, Hong Kong, and the US, but not in Korea.

## 448 Data processing

449 For all time series, we rounded every year to 52 weeks by taking the average number  
450 of cases and tests between the 52nd and 53rd week. We also rescaled all time series to  
451 account for changes in testing patterns, which were then used for the actual analysis.

452 For Canada, an increase in testing was observed from 2013 to 2024 (Supplemen-  
453 tary Figure S17). To account for this increase, we calculated a 2 year moving average  
454 for the number of tests for each pathogen, which we used as a proxy for testing effort.  
455 Then, we divided the smoothed testing patterns by the smoothed value at the final  
456 week such that the testing effort has a maximum of 1. We then divided weekly cases  
457 by the testing effort to obtain a scaled case time series. A similar approach was used  
458 earlier for an analysis of RSV time series in the US to account for changes in testing  
459 patterns [26].

460 For Hong Kong, we applied the same scaling procedure to the time series as we  
461 did for Canada. In this case, we only adjusted for testing efforts up to the end of 2019  
462 because there was a major reduction in testing for common respiratory pathogens  
463 between 2020 and 2023 (Supplementary Figure S18).

464 For Korea, while we did not have information on testing, the reported number  
465 of respiratory infections consistently increased from 2013 to the end of 2019, which  
466 we interpreted as changes in testing patterns (Supplementary Figure S19). Since  
467 we did not have testing numbers, we used the weekly sum of all acute respiratory  
468 viral infection cases as a proxy for testing, which were further smoothed with moving  
469 average and scaled to have a maximum of 1. For Korea, we also only adjusted for  
470 testing efforts up to the end of 2019.

471 In the US, there has been a large increase in testing for some respiratory pathogens,  
472 especially RSV, which could not be corrected by simple scaling (Supplementary Fig-  
473 ure S20). Instead, we derived an incidence proxy by multiplying the test positivity  
474 with influenza-like illness positivity, which was taken from [https://gis.cdc.gov/](https://gis.cdc.gov/grasp/fluview/fluportaldashboard.html)  
475 [grasp/fluview/fluportaldashboard.html](https://gis.cdc.gov/grasp/fluview/fluportaldashboard.html). This method of estimating an inci-  
476 dence proxy has been recently applied in the analysis of seasonal coronaviruses [7]  
477 and *Mycoplasma pneumoniae* infections [4]. Detailed assumptions and justifications  
478 are provided in [41].

## 479 Data summary

480 To make qualitative comparisons between pre- and post-perturbation dynamics of  
481 respiratory pathogen circulation patterns, we calculated the mean seasonal patterns  
482 using time series of either rescaled cases or incidence proxy estimates before 2020. We  
483 did so by taking the mean value in each week across all years before 2020. Confidence  
484 intervals around the means were calculated using a simple t test.

485 **Estimating pathogen resilience**

486 In order to measure pathogen resilience from surveillance data, we first reconstructed  
 487 the empirical pre-pandemic attractor of the system using Takens' embedding theorem  
 488 [17]. Specifically, for a given pathogen, we took the pre-pandemic (before 2020) case  
 489 time series  $C(t)$  and reconstructed the attractor using delayed embedding with a  
 490 uniform delay of  $\tau$  and dimension  $M$ :

$$X_{\tau,m}(t) = \langle \log(C(t) + 1), \log(C(t - \tau) + 1), \dots, \log(C(t - (M - 1)\tau) + 1) \rangle. \quad (2)$$

491 Here, the delay  $\tau$  was determined by calculating the autocorrelation of the logged  
 492 pre-pandemic time series and asking when the autocorrelation crosses 0 for the first  
 493 time [22]; a typical delay for an annual outbreak is around 13 weeks.

494 Then, for a given delay  $\tau$ , we determined the embedding dimension  $M$  using the  
 495 false nearest neighbors approach [21, 22]. To do so, we started with an embedding  
 496 dimension  $e$  and constructed a set of points  $A_{\tau,e} = \{X_{\tau,e}(t) | t < 2020\}$ . Then, for  
 497 each point  $X_{\tau,e}(t)$ , we determined the nearest neighbor from the set  $A_{\tau,e}$ , which we  
 498 denote  $X_{\tau,e}(t_{nn})$  for  $t \neq t_{nn}$ . Then, if the distance between these two points in the  
 499  $e+1$  dimension,  $D_{\tau,e+1}(t) = \|X_{\tau,e+1}(t_{nn}) - X_{\tau,e+1}(t)\|_2$ , is larger than their distance in  
 500 the  $e$  dimension,  $D_{\tau,e}(t) = \|X_{\tau,e}(t_{nn}) - X_{\tau,e}(t)\|_2$ , these two points are deemed to be  
 501 false nearest neighbors; specifically, we used a threshold  $R$  for the ratio between two  
 502 distances  $D_{\tau,e+1}(t)/D_{\tau,e}(t)$  to determine false nearest neighbors. The first embed-  
 503 ding dimension  $e$  that does not have any false nearest neighbors corresponds to the  
 504 embedding dimension  $M$  for a given pathogen-country pair. For the main analysis,  
 505 we used  $R = 10$ , which was chosen from a sensitivity analysis against simulated data  
 506 (Supplementary Text). Once we determined the embedding lag  $\tau$  and dimension  $M$ ,  
 507 we apply the embedding to the entire time series and calculate the nearest neigh-  
 508 bor distance against the attractor  $A_{\tau,M}$  to obtain a time series of distance from the  
 509 attractor  $D_{\tau,M}(t)$ .

510 From a time series of distances from the attractor, we estimated pathogen re-  
 511 silience by fitting a linear regression to an appropriate window. To automatically  
 512 select fitting windows, we began by smoothing the distance time series using locally  
 513 estimated scatterplot smoothing (LOESS) to obtain  $\hat{D}_{\tau,M}(t)$ , where the smoothing  
 514 is performed on a log scale and exponentiated afterwards. This smoothing allowed  
 515 us to find appropriate threshold values for selecting fitting windows that are insensi-  
 516 tive to errors in our estimates of distance from the attractor. Then, we determined  
 517 threshold values ( $T_{\text{start}}$  and  $T_{\text{end}}$ ) for the smoothed distances and choose the fitting  
 518 window based on when  $\hat{D}_{\tau,M}(t)$  crosses these threshold values for the first time.  
 519 These thresholds were determined by first calculating the maximum distance,

$$\max \hat{D} = \max \hat{D}_{\tau,M}(t), \quad (3)$$

520 and the mean pre-pandemic distance,

$$\hat{D}_{\text{mean}} = \frac{1}{N_{t < 2020}} \sum_{t < 2020} \hat{D}_{\tau,M}(t), \quad (4)$$

521 as a reference, and then dividing their ratios into  $K$  equal bins,

$$T_{\text{start}} = \hat{D}_{\text{mean}} \times \left( \frac{\max \hat{D}}{\hat{D}_{\text{mean}}} \right)^{(K-a)/K}, \quad (5)$$

$$T_{\text{end}} = \hat{D}_{\text{mean}} \times \left( \frac{\max \hat{D}}{\hat{D}_{\text{mean}}} \right)^{a/K}, \quad (6)$$

522 where  $a$  represents the truncation threshold. This allows us to discard the initial  
 523 period during which the distance increases (from the introduction of intervention  
 524 measures) and the final period during which the distance plateaus (as the system  
 525 reaches an attractor). The fitting window is determined based on when the smoothed  
 526 distance  $\hat{D}_{\tau,M}(t)$  crosses these threshold values for the first time; then, we fit a  
 527 linear regression to logged (unsmoothed) distances  $\log D_{\tau,M}(t)$  using that window.  
 528 Alongside the threshold  $R$  for the false nearest neighbors approach, we tested optimal  
 529 choices for  $K$  and  $a$  values using simulations (Supplementary Text). We used  $K = 19$   
 530 and  $a = 2$  throughout the paper based on the simulation results.

## 531 Mathematical modeling

532 Throughout the paper, we use a series of mathematical models to illustrate the  
 533 concept of pathogen resilience and to understand the determinants of pathogen re-  
 534 silience. In general, the intrinsic resilience of a given system is given by the largest  
 535 real part of the eigenvalues of the linearized system at endemic equilibrium. Here, we  
 536 focus on the SIRS model with demography (birth and death) and present the details  
 537 of other models in Supplementary Text. The SIRS (Susceptible-Infected-Recovered-  
 538 Susceptible) model is the simplest model that allows for waning of immunity, where  
 539 recovered (immune) individuals are assumed to become fully susceptible after an  
 540 average of  $1/\delta$  time period. The dynamics of the SIRS model is described by the  
 541 following set of differential equations:

$$\frac{dS}{dt} = \mu - \beta(t)SI - \mu S + \delta R \quad (7)$$

$$\frac{dI}{dt} = \beta(t)SI - (\gamma + \mu)I \quad (8)$$

$$\frac{dR}{dt} = \gamma I - (\delta + \mu)R \quad (9)$$

542 where  $\mu$  represents the birth and death rates,  $\beta(t)$  represents the time-varying trans-  
 543 mission rate, and  $\gamma$  represents the recovery rate. The basic reproduction number  
 544  $\mathcal{R}_0(t) = \beta(t)/(\gamma + \mu)$  is defined as the average number of secondary infections that  
 545 a single infected individual would cause in a fully susceptible population at time  $t$   
 546 and measures the intrinsic transmissibility of a pathogen.

547 When we introduced the idea of pathogen resilience (Figure 2), we imposed sinu-  
 548 soidal changes to the transmission rate to account for seasonal transmission,

$$\beta(t) = b_1(1 + \theta \cos(2\pi(t - \phi)))\alpha(t), \quad (10)$$

549 where  $b_1$  represents the baseline transmission rate,  $\theta$  represents the seasonal ampli-  
 550 tude, and  $\phi$  represents the seasonal offset term. Here, we also introduced an extra  
 551 multiplicative term  $\alpha(t)$  to account for the impact of pandemic perturbations, where  
 552  $\alpha(t) < 1$  indicates transmission reduction. Figure 2A and 2B were generated assum-  
 553 ing  $b_1 = 3 \times (365/7 + 1/50)/\text{years}$ ,  $\theta = 0.2$ ,  $\phi = 0$ ,  $\mu = 1/50/\text{years}$ ,  $\gamma = 365/7/\text{years}$ ,  
 554 and  $\delta = 1/2/\text{years}$ . Specifically,  $b_1 = 3 \times (365/7 + 1/50)/\text{years}$  implies  $\mathcal{R}_0 = 3$ , where  
 555  $(365/7 + 1/50)/\text{years}$  represent the rate of recovery. In Figure 2A, we imposed a 50%  
 556 transmission reduction for 6 months from 2020:

$$\alpha(t) = \begin{cases} 0.5 & 2020 \leq t < 2020.5 \\ 1 & \text{otherwise} \end{cases} \quad (11)$$

557 In Figure 2B, we imposed a 50% transmission reduction for 6 months from 2020 and  
 558 a permanent 10% reduction onward:

$$\alpha(t) = \begin{cases} 1 & t < 2020 \\ 0.5 & 2020 \leq t < 2020.5 \\ 0.9 & 2020.5 \leq t \end{cases} \quad (12)$$

559 In both scenarios, we simulated the SIRS model from the same initial conditions  
 560 ( $S(0) = 1/\mathcal{R}_0$ ,  $I(0) = 1 \times 10^{-6}$ , and  $R(0) = 1 - S(0) - I(0)$ ) from 1900 until 2030.  
 561 Throughout the paper, all deterministic models were solved using the `lsoda` solver  
 562 from the `deSolve` package [42] in R [43].

563 To measure the empirical resilience of the SIRS model (Figure 2C and 2F), we  
 564 computed the normalized distance between post-intervention susceptible and logged  
 565 infected proportions and their corresponding unperturbed values at the same time:

$$\sqrt{\left(\frac{S(t) - S_{\text{unperturbed}}(t)}{\sigma_S}\right)^2 + \left(\frac{\log I(t) - \log I_{\text{unperturbed}}(t)}{\sigma_{\log I}}\right)^2}, \quad (13)$$

566 where  $\sigma_S$  and  $\sigma_{\log I}$  represent the standard deviation in the unperturbed susceptible  
 567 and logged infected proportions. The unperturbed values were obtained by simula-  
 568 ting the same SIRS model without pandemic perturbations ( $\alpha = 1$ ). We normalized  
 569 the differences in susceptible and logged infected proportions to allow both quantities  
 570 to equally contribute to the changes in distance from the attractor. We used logged  
 571 prevalence, instead of absolute prevalence, in order to capture epidemic dynamics  
 572 in deep troughs during the intervention period. In Supplementary Materials, we  
 573 also compared how the degree of seasonal transmission affects empirical resilience  
 574 by varying  $\theta$  from 0 to 0.4; when we assumed no seasonality ( $\theta = 0$ ), we did not

575 normalize the distance because the standard deviation of pre-intervention dynamics  
576 are zero.

577 We used the SIRS model to understand how underlying epidemiological parameters  
578 affect pathogen resilience and determine the relationship to underlying sus-  
579 ceptible host dynamics. For the simple SIRS model without seasonal transmission  
580 ( $\theta = 0$ ), the intrinsic resilience equals

$$-\frac{\text{Re}(\lambda)}{2} = \frac{\delta + \beta I^* + \mu}{2}. \quad (14)$$

581 Here,  $I^*$  represents the prevalence at endemic equilibrium:

$$I^* = \frac{(\delta + \mu)(\beta - (\gamma + \mu))}{\beta(\delta + \gamma + \mu)}. \quad (15)$$

582 The susceptible replenishment rate is given by

$$S_{\text{replenish}} = \frac{\mu + \delta R}{S^*}, \quad (16)$$

583 where  $S^* = 1/\mathcal{R}_0$  represents the equilibrium proportion of susceptible individuals.  
584 We varied the basic reproduction number  $\mathcal{R}_0$  between 1.1 to 6 and the average  
585 duration of immunity  $1/\delta$  between 2 to 4 years, and computed these two quantities.  
586 In doing so, we fixed all other parameters:  $\mu = 1/80/\text{years}$  and  $\gamma = 365/7/\text{years}$ .  
587 When infection provides a life-long immunity ( $\delta = 0$ ), the intrinsic resilience is  
588 inversely proportional to the susceptible replenishment rate:

$$-\frac{\text{Re}(\lambda)}{2} = \frac{\mu}{2S^*} = \frac{S_{\text{replenish}}}{2}. \quad (17)$$

589 Finally, we used a seasonally unforced stochastic SIRS model without demog-  
590 raphy to understand how pathogen resilience affects sensitivity of the system to  
591 demographic stochasticity (see Supplementary Text for the details of the stochas-  
592 tic SIRS model). By varying the basic reproduction number  $\mathcal{R}_0$  between 2 to 20  
593 and the average duration of immunity  $1/\delta$  between 1 to 40 years, we ran the SIRS  
594 model for 100 years and computed the epidemic amplitude, which we defined as  
595  $(\max I - \min I)/(2\bar{I})$ . Each simulation began from the equilibrium, and we trun-  
596 cated the initial 25 years before computing the epidemic amplitude. In doing so,  
597 we assumed  $\gamma = 365/7/\text{years}$  and fixed the population size to 1 billion to prevent  
598 any fadeouts. We also considered a seasonally forced stochastic SIRS model without  
599 demography, assuming an amplitude of seasonal forcing of 0.04; in this case, we com-  
600 puted the relative epidemic amplitude by comparing the deterministic and stochastic  
601 trajectories (Supplementary Materials).

## 602 Data availability

603 All data and code are stored in a publicly available GitHub repository (<https://github.com/cobeylab/return-time>).

605 **Funding**

606 S.W.P. is a Peter and Carmen Lucia Buck Foundation Awardee of the Life Sciences  
607 Research Foundation. S.C. was supported by Federal funds from the National Insti-  
608 tute of Allergy and Infectious Diseases, National Institutes of Health, Department of  
609 Health and Human Services under CEIRR contract 75N93021C00015. The content is  
610 solely the responsibility of the authors and does not necessarily represent the official  
611 views of the NIAID or the National Institutes of Health.

612 **Supplementary Text**

613 **Resilience of a stage-structured system.**

614 In Figure 2G–I, we used a more realistic, stage-structured model to illustrate how  
 615 transient phenomena can cause the system to slow down. Specifically, we used the  
 616 stage-structured RSV model proposed by [26], which assumes that subsequent rein-  
 617 fections cause an individual to become less susceptible and transmissible than previ-  
 618 ous infections. In contrast to a standard SIRS model, this model does not include a  
 619 recovered compartment, which allow for temporary protection against new infections,  
 620 and assumes that recovered individuals are immediately susceptible to new infections.  
 621 The model dynamics can be described as follows:

$$\frac{dM}{dt} = \mu - (\omega + \mu)M \quad (S1)$$

$$\frac{dS_0}{dt} = \omega M - (\lambda(t) + \mu)S_0 \quad (S2)$$

$$\frac{dI_1}{dt} = \lambda(t)S_0 - (\gamma_1 + \mu)I_1 \quad (S3)$$

$$\frac{dS_1}{dt} = \gamma_1 I_1 - (\sigma_1 \lambda(t) + \mu)S_1 \quad (S4)$$

$$\frac{dI_2}{dt} = \sigma_1 \lambda(t)S_1 - (\gamma_2 + \mu)I_2 \quad (S5)$$

$$\frac{dS_2}{dt} = \gamma_2 I_2 - (\sigma_2 \lambda(t) + \mu)S_2 \quad (S6)$$

$$\frac{dI_3}{dt} = \sigma_2 \lambda(t)S_2 - (\gamma_3 + \mu)I_3 \quad (S7)$$

$$\frac{dS_3}{dt} = \gamma_3 I_3 - (\sigma_3 \lambda(t) + \mu)S_3 + \gamma_4 I_4 \quad (S8)$$

$$\frac{dI_4}{dt} = \sigma_3 \lambda(t)S_3 - (\gamma_4 + \mu)I_4 \quad (S9)$$

622 where  $M$  represents the proportion of individuals who are maternally immune;  $S_i$   
 623 represents the proportion of individuals who are susceptible after  $i$  prior infections;  $I_i$   
 624 represents the proportion of individuals who are currently (re)-infected with their  $i$ -th  
 625 infection;  $\mu$  represents the birth and death rates;  $1/\omega$  represents the mean duration  
 626 of maternal immunity;  $1/\gamma_i$  represents the mean duration of infection;  $\lambda(t)$  represents  
 627 the force of infection; and  $\sigma_i$  represents the reduction in susceptibility for the  $i$ -th  
 628 reinfection. The force of infection is modeled using a sinusoidal function:

$$\beta(t) = b_1(1 + \theta \cos(2\pi(t - \phi)))\alpha(t) \quad (S10)$$

$$\lambda(t) = \beta(I_1 + \rho_1 I_2 + \rho_2(I_3 + I_4)), \quad (S11)$$

629 where  $b_1$  represents the baseline transmission rate;  $\theta$  represents the seasonal ampli-  
 630 tude;  $\phi$  represents the seasonal offset term;  $\alpha(t)$  represents the intervention effect;

and  $\rho_i$  represents the impact of immunity on transmission reduction. We used the following parameters to simulate the impact of interventions on epidemic dynamics [26]:  $b_1 = 9 \times (365/10 + 1/80)/\text{years}$ ,  $\theta = 0.2$ ,  $\phi = -0.1$ ,  $\omega = 365/112/\text{years}$ ,  $\gamma_1 = 365/10/\text{years}$ ,  $\gamma_2 = 365/7/\text{years}$ ,  $\gamma_3 = 365/5/\text{years}$ ,  $\sigma_1 = 0.76$ ,  $\sigma_2 = 0.6$ ,  $\sigma_3 = 0.4$ ,  $\rho_1 = 0.75$ ,  $\rho_2 = 0.51$ , and  $\mu = 1/80/\text{years}$ . We assumed a 50% transmission reduction for 6 months from 2020:

$$\alpha(t) = \begin{cases} 0.5 & 2020 \leq t < 2020.5 \\ 1 & \text{otherwise} \end{cases} \quad (\text{S12})$$

The model was simulated from 1900 to 2030 using the following initial conditions:  $M = 0$ ,  $S_0 = 1/\mathcal{R}_0 - I_1$ ,  $I_1 = 1 \times 10^{-6}$ ,  $S_1 = 1 - 1/\mathcal{R}_0$ ,  $I_2 = 0$ ,  $S_2 = 0$ ,  $I_3 = 0$ ,  $S_3 = 0$ , and  $I_4 = 0$ . For the phase plane analysis (Figure 2H) and distance analysis (Figure 2I), we relied on the average susceptibility,

$$\bar{S} = S_0 + \sigma_1 S_1 + \sigma_2 S_2 + \sigma_3 S_3, \quad (\text{S13})$$

and total prevalence,

$$I_{\text{total}} = I_1 + I_2 + I_3 + I_4. \quad (\text{S14})$$

These quantities were used to compute the normalized distance from the attractor, as described in the main text.

## Resilience of a multistain system.

We used a simple two-strain model to show that a multistain host-pathogen system that is coupled through cross immunity can be described by a single resilience value. The model dynamics can be described as follows [33]:

$$\frac{dS}{dt} = \mu - \mu S - (\lambda_1 + \lambda_2)S + \delta_1 R_1 + \delta_2 R_2 \quad (\text{S15})$$

$$\frac{dI_1}{dt} = \lambda_1 S - (\gamma_1 + \mu)I_1 \quad (\text{S16})$$

$$\frac{dI_2}{dt} = \lambda_2 S - (\gamma_2 + \mu)I_2 \quad (\text{S17})$$

$$\frac{dR_1}{dt} = \gamma_1 I_1 - \lambda_2 \epsilon_{21} R_1 - \delta_1 R_1 + \delta_2 R - \mu R_1 \quad (\text{S18})$$

$$\frac{dR_2}{dt} = \gamma_2 I_2 - \lambda_1 \epsilon_{12} R_2 - \delta_2 R_2 + \delta_1 R - \mu R_2 \quad (\text{S19})$$

$$\frac{dJ_1}{dt} = \lambda_1 \epsilon_{12} R_2 - (\gamma_1 + \mu) J_1 \quad (\text{S20})$$

$$\frac{dJ_2}{dt} = \lambda_2 \epsilon_{21} R_1 - (\gamma_2 + \mu) J_2 \quad (\text{S21})$$

$$\frac{dR}{dt} = \gamma_1 J_1 + \gamma_2 J_2 - \delta_1 R - \delta_2 R - \mu R \quad (\text{S22})$$

648 where  $S$  represents the proportion of individuals who are fully susceptible to infections  
 649 by both strains;  $I_1$  represents the proportion of individuals who are infected  
 650 with strain 1 without prior immunity;  $I_2$  represents the proportion of individuals who  
 651 are infected with strain 2 without prior immunity;  $R_1$  represents the proportion of  
 652 individuals who are fully immune against strain 1 and partially susceptible to rein-  
 653 fection by strain 2;  $R_2$  represents the proportion of individuals who are fully immune  
 654 against strain 2 and partially susceptible to reinfection by strain 1;  $J_1$  represents the  
 655 proportion of individuals who are infected with strain 1 with prior immunity against  
 656 strain 2;  $J_2$  represents the proportion of individuals who are infected with strain  
 657 2 with prior immunity against strain 1;  $R$  represents the proportion of individuals  
 658 who are immune to infections from both strains;  $\mu$  represents the birth/death rate;  
 659  $\lambda_1$  and  $\lambda_2$  represent the force of infection from strains 1 and 2, respectively;  $\delta_1$  and  
 660  $\delta_2$  represent the waning immunity rate;  $\gamma_1$  and  $\gamma_2$  represent the recovery rate;  $\epsilon_{21}$   
 661 and  $\epsilon_{12}$  represent the susceptibility to reinfection with strains 2 and 1, respectively,  
 662 given prior immunity from infection with strains 1 and 2, respectively. The force of  
 663 infection is modeled as follows:

$$\beta_1 = b_1(1 + \theta_1 \sin(2\pi(t - \phi_1)))\alpha(t) \quad (\text{S23})$$

$$\beta_2 = b_2(1 + \theta_2 \sin(2\pi(t - \phi_2)))\alpha(t) \quad (\text{S24})$$

$$\lambda_1 = \beta_1(I_1 + J_1) \quad (\text{S25})$$

$$\lambda_2 = \beta_2(I_2 + J_2) \quad (\text{S26})$$

664 In Supplementary Figures S2–S4, we assumed the following parameters:  $b_1 = 2 \times$   
 665 52/years,  $b_2 = 4 \times 52/\text{years}$ ,  $\phi_1 = \phi_2 = 0$ ,  $\epsilon_{12} = 0.9$ ,  $\epsilon_{21} = 0.5$ ,  $\gamma_1 = \gamma_2 = 52/\text{years}$ ,  
 666  $\delta_1 = \delta_2 = 1/\text{years}$ , and  $\mu = 1/70/\text{years}$ . For all simulations, we assumed a 50%  
 667 transmission reduction for 6 months from 2020:

$$\alpha(t) = \begin{cases} 0.5 & 2020 \leq t < 2020.5 \\ 1 & \text{otherwise} \end{cases} \quad (\text{S27})$$

668 The seasonal amplitude  $\theta$  is varied from 0 to 0.4. All simulations were run from 1900  
 669 to 2030 with following initial conditions:  $S(0) = 1 - 2 \times 10^{-6}$ ,  $I_1(0) = 1 \times 10^{-6}$ ,  
 670  $I_2(0) = 1 \times 10^{-6}$ ,  $R_1(0) = 0$ ,  $R_2(0) = 0$ ,  $J_1(0) = 0$ ,  $J_2(0) = 0$ , and  $R(0) = 0$ .

671 We considered three scenarios for measuring pathogen resilience: (1) we only have  
 672 information about strain 1, (2) we only have information about strain 2, and (3) we  
 673 are unable to distinguish between strains. In the first two scenarios (see panels A–C  
 674 for strain 1 and panels D–F for strain 2), we considered the dynamics of average  
 675 susceptibility for each strain and total prevalence:

$$\bar{S}_1 = S + \epsilon_{12}R_2 \quad (\text{S28})$$

$$\hat{I}_1 = I_1 + J_1 \quad (\text{S29})$$

$$\bar{S}_2 = S + \epsilon_{21}R_1 \quad (\text{S30})$$

$$\hat{I}_2 = I_2 + J_2 \quad (\text{S31})$$

676 In the third scenario (panels G–I), we considered the dynamics of total susceptible  
677 and infected populations:

$$\hat{S} = S + R_2 + R_1 \quad (\text{S32})$$

$$\hat{I} = I_1 + J_1 + I_2 + J_2 \quad (\text{S33})$$

678 These quantities were used to compute the normalized distance from the attractor,  
679 as described in the main text.

## 680 Estimating intrinsic resilience using a mechanistic model

681 We tested whether we can reliably estimate the intrinsic resilience of a system by fit-  
682 ting a mechanistic model. Specifically, we simulated case time series from stochastic  
683 SIRS and two-strain models and fitted a simple, deterministic SIRS model using a  
684 Bayesian framework [4, 23, 44].

685 We simulated the models in discrete time with a daily time step ( $\Delta t = 1$ ),  
686 incorporating demographic stochasticity:

$$\beta(t) = \mathcal{R}_0 \left( 1 + \theta \cos \left( \frac{2\pi t}{364} \right) \right) \alpha(t)(1 - \exp(-\gamma)) \quad (\text{S34})$$

$$\text{FOI}(t) = \beta(t)I(t - \Delta t)/N \quad (\text{S35})$$

$$B(t) \sim \text{Poisson}(\mu N) \quad (\text{S36})$$

$$\Delta S(t) \sim \text{Binom}(S(t - \Delta t), 1 - \exp(-(\text{FOI}(t) + \mu)\Delta t)) \quad (\text{S37})$$

$$N_{SI}(t) \sim \text{Binom}\left(\Delta S(t), \frac{\text{FOI}(t)}{\text{FOI}(t) + \mu}\right) \quad (\text{S38})$$

$$\Delta I(t) \sim \text{Binom}(I(t - \Delta t), 1 - \exp(-(\gamma + \mu)\Delta t)) \quad (\text{S39})$$

$$N_{IR}(t) \sim \text{Binom}\left(\Delta I(t), \frac{\gamma}{\gamma + \mu}\right) \quad (\text{S40})$$

$$\Delta R(t) \sim \text{Binom}(R(t - \Delta t), 1 - \exp(-(\delta + \mu)\Delta t)) \quad (\text{S41})$$

$$N_{RS}(t) \sim \text{Binom}\left(\Delta R(t), \frac{\delta}{\delta + \mu}\right) \quad (\text{S42})$$

$$S(t) = S(t - \Delta t) + N_{RS}(t) + B(t) - \Delta S(t) \quad (\text{S43})$$

$$I(t) = I(t - \Delta t) + N_{SI}(t) - \Delta I(t) \quad (\text{S44})$$

$$R(t) = R(t - \Delta t) + N_{IR}(t) - \Delta R(t) \quad (\text{S45})$$

687 where FOI represents the force of infection;  $N_{ij}$  represents the number of individuals  
688 moving from compartment  $i$  to  $j$  on a given day; and  $B(t)$  represents the number  
689 of new births. All other parameters definitions can be found in the description of  
690 the deterministic version of the model. We simulated the model on a daily scale—  
691 assuming 364 days in a year so that it can be evenly grouped into 52 weeks—with  
692 the following parameters:  $\mathcal{R}_0 = 3$ ,  $\theta = 0.1$ ,  $\gamma = 1/7/\text{days}$ ,  $\delta = 1/(364 \times 2)/\text{days}$ ,

<sup>693</sup>  $\mu = 1/(364 \times 50)$ /days, and  $N = 1 \times 10^8$ . The model was simulated from 1900 to  
<sup>694</sup> 2030 assuming  $S(0) = N/3$ ,  $I(0) = 100$ , and  $R(0) = N - S(0) - I(0)$ . The observed  
<sup>695</sup> incidence from the model was then simulated as follows:

$$C(t) = \text{Beta-Binom}(N_{SI}(t), \rho, k), \quad (\text{S46})$$

<sup>696</sup> where  $\rho$  represents the reporting probability and  $k$  represents the overdispersion  
<sup>697</sup> parameter of beta-binomial distribution. Here, we used the beta-binomial distribu-  
<sup>698</sup> tion to account for overdispersion in reporting. We assumed  $\rho = 0.002$  (i.e., 0.2%  
<sup>699</sup> probability) and  $k = 1000$ .

<sup>700</sup> We used an analogous approach for the two-strain model:

$$\beta_1(t) = b_1 \left( 1 + \theta_1 \cos \left( \frac{2\pi(t - \phi_1)}{364} \right) \right) \alpha(t) \quad (\text{S47})$$

$$\beta_2(t) = b_2 \left( 1 + \theta_2 \cos \left( \frac{2\pi(t - \phi_2)}{364} \right) \right) \alpha(t) \quad (\text{S48})$$

$$\text{FOI}_1(t) = \beta_1(t)(I_1(t - \Delta t) + J_1(t - \Delta t))/N \quad (\text{S49})$$

$$\text{FOI}_2(t) = \beta_2(t)(I_2(t - \Delta t) + J_2(t - \Delta t))/N \quad (\text{S50})$$

$$B(t) \sim \text{Poisson}(\mu N) \quad (\text{S51})$$

$$\Delta S(t) \sim \text{Binom}(S(t - \Delta t), 1 - \exp(-(\text{FOI}_1(t) + \text{FOI}_2(t) + \mu)\Delta t)) \quad (\text{S52})$$

$$N_{SI_1}(t) \sim \text{Binom}\left(\Delta S(t), \frac{\text{FOI}_1(t)}{\text{FOI}_1(t) + \text{FOI}_2(t) + \mu}\right) \quad (\text{S53})$$

$$N_{SI_2}(t) \sim \text{Binom}\left(\Delta S(t), \frac{\text{FOI}_2(t)}{\text{FOI}_1(t) + \text{FOI}_2(t) + \mu}\right) \quad (\text{S54})$$

$$\Delta I_1(t) \sim \text{Binom}(I_1(t - \Delta t), 1 - \exp(-(\gamma_1 + \mu)\Delta t)) \quad (\text{S55})$$

$$N_{I_1 R_1}(t) \sim \text{Binom}\left(\Delta I_1(t), \frac{\gamma_1}{\gamma_1 + \mu}\right) \quad (\text{S56})$$

$$\Delta I_2(t) \sim \text{Binom}(I_2(t - \Delta t), 1 - \exp(-(\gamma_2 + \mu)\Delta t)) \quad (\text{S57})$$

$$N_{I_2 R_2}(t) \sim \text{Binom}\left(\Delta I_2(t), \frac{\gamma_2}{\gamma_2 + \mu}\right) \quad (\text{S58})$$

$$\Delta R_1(t) \sim \text{Binom}(R_1(t - \Delta t), 1 - \exp(-(\epsilon_{21}\text{FOI}_2(t) + \rho_1 + \mu)\Delta t)) \quad (\text{S59})$$

$$N_{R_1 S}(t) \sim \text{Binom}\left(\Delta R_1(t), \frac{\rho_1}{\epsilon_{21}\text{FOI}_2(t) + \rho_1 + \mu}\right) \quad (\text{S60})$$

$$N_{R_1 J_2}(t) \sim \text{Binom}\left(\Delta R_1(t), \frac{\epsilon_{21}\text{FOI}_2(t)}{\epsilon_{21}\text{FOI}_2(t) + \rho_1 + \mu}\right) \quad (\text{S61})$$

$$\Delta R_2(t) \sim \text{Binom}(R_2(t - \Delta t), 1 - \exp(-(\epsilon_{12}\text{FOI}_1(t) + \rho_2 + \mu)\Delta t)) \quad (\text{S62})$$

$$N_{R_2 S}(t) \sim \text{Binom}\left(\Delta R_2(t), \frac{\rho_2}{\epsilon_{12}\text{FOI}_1(t) + \rho_2 + \mu}\right) \quad (\text{S63})$$

$$N_{R_2 J_1}(t) \sim \text{Binom}\left(\Delta R_2(t), \frac{\epsilon_{12}\text{FOI}_1(t)}{\epsilon_{12}\text{FOI}_1(t) + \rho_2 + \mu}\right) \quad (\text{S64})$$

$$\Delta J_1(t) \sim \text{Binom}(J_1(t - \Delta t), 1 - \exp(-(\gamma_1 + \mu)\Delta t)) \quad (\text{S65})$$

$$N_{J_1R}(t) \sim \text{Binom}\left(\Delta J_1(t), \frac{\gamma_1}{\gamma_1 + \mu}\right) \quad (\text{S66})$$

$$\Delta J_2(t) \sim \text{Binom}(J_2(t - \Delta t), 1 - \exp(-(\gamma_2 + \mu)\Delta t)) \quad (\text{S67})$$

$$N_{J_2R}(t) \sim \text{Binom}\left(\Delta J_2(t), \frac{\gamma_2}{\gamma_2 + \mu}\right) \quad (\text{S68})$$

$$\Delta R(t) \sim \text{Binom}(R(t - \Delta t), 1 - \exp(-(\rho_1 + \rho_2 + \mu)\Delta t)) \quad (\text{S69})$$

$$N_{RR_1}(t) \sim \text{Binom}\left(\Delta R(t), \frac{\rho_1}{\rho_1 + \rho_2 + \mu}\right) \quad (\text{S70})$$

$$N_{RR_2}(t) \sim \text{Binom}\left(\Delta R(t), \frac{\rho_2}{\rho_1 + \rho_2 + \mu}\right) \quad (\text{S71})$$

$$S(t) = S(t - \Delta t) - \Delta S(t) + B(t) + N_{R_1S}(t) + N_{R_2S}(t) \quad (\text{S72})$$

$$I_1(t) = I_1(t - \Delta t) - \Delta I_1(t) + N_{SI_1}(t) \quad (\text{S73})$$

$$I_2(t) = I_2(t - \Delta t) - \Delta I_2(t) + N_{SI_2}(t) \quad (\text{S74})$$

$$R_1(t) = R_1(t - \Delta t) - \Delta R_1(t) + N_{I_1R_1}(t) + N_{RR_1}(t) \quad (\text{S75})$$

$$R_2(t) = R_2(t - \Delta t) - \Delta R_2(t) + N_{I_2R_2}(t) + N_{RR_2}(t) \quad (\text{S76})$$

$$J_1(t) = J_1(t - \Delta t) - \Delta J_1(t) + N_{R_2J_1}(t) \quad (\text{S77})$$

$$J_2(t) = J_2(t - \Delta t) - \Delta J_2(t) + N_{R_1J_2}(t) \quad (\text{S78})$$

$$R(t) = R(t - \Delta t) - \Delta R(t) + N_{J_1R}(t) + N_{J_2R}(t) \quad (\text{S79})$$

We simulated the model on a daily scale with previously estimated parameters for the RSV-HMPV interaction [33]:  $b_1 = 1.7/\text{weeks}$ ,  $b_2 = 1.95/\text{weeks}$ ,  $\theta_1 = 0.4$ ,  $\theta_2 = 0.3$ ,  $\phi_1 = 0.005 \times 7/364$ ,  $\phi_2 = 4.99 \times 7/364$ ,  $\epsilon_{12} = 0.92$ ,  $\epsilon_{21} = 0.45$ ,  $\gamma_1 = 1/10/\text{days}$ ,  $\gamma_2 = 1/10/\text{days}$ ,  $\rho_1 = 1/364/\text{days}$ ,  $\rho_2 = 1/364/\text{days}$ ,  $\mu = 1/(70 \times 364)/\text{days}$ , and  $N = 1 \times 10^8$ . The model was simulated from 1900 to 2030 assuming  $S(0) = N - 200$ ,  $I_1(0) = 100$ ,  $I_2(0) = 100$ ,  $R_1(0) = 0$ ,  $R_2(0) = 0$ ,  $J_1(0) = 0$ ,  $J_2(0) = 0$ , and  $R(0) = 0$ . The observed incidence for each strain is then simulated as follows:

$$C_1(t) = \text{Beta-Binom}(N_{SI_1}(t) + N_{R_2J_1}, \rho, k), \quad (\text{S80})$$

$$C_2(t) = \text{Beta-Binom}(N_{SI_2}(t) + N_{R_1J_2}, \rho, k), \quad (\text{S81})$$

where  $\rho$  represents the reporting probability and  $k$  represents the overdispersion parameter of beta-binomial distribution. We assumed  $\rho = 0.002$  (i.e., 0.2% probability) and  $k = 500$ . We also considered the total incidence:  $C_{\text{total}}(t) = C_1(t) + C_2(t)$ .

For both models, we considered a more realistically shaped pandemic perturbation  $\alpha(t)$  to challenge our ability to estimate the intervention effects. Thus, we assumed a 40% transmission reduction for 3 months from March 2020, followed by a 10% transmission reduction for 6 months, 20% transmission reduction for 3 months,

715 and a final return to normal levels:

$$\alpha(t) = \begin{cases} 1 & t < 2020.25 \\ 0.6 & 2020.25 \leq t < 2020.5 \\ 0.9 & 2020.5 \leq t < 2021 \\ 0.8 & 2021 \leq t < 2021.25 \\ 1 & 2021.25 \leq t \end{cases}. \quad (\text{S82})$$

716 For all simulations, we truncated the time series from the beginning of 2014 to the  
717 end of 2023 and aggregated them into weekly cases.

718 To infer intrinsic resilience from time series, we fitted a simple discrete time,  
719 deterministic SIRS model in a Bayesian framework [4]:

$$\Delta t = 1 \text{ week} \quad (\text{S83})$$

$$\text{FOI}(t) = \beta(t)(I(t - \Delta t) + \omega)/N \quad (\text{S84})$$

$$\Delta S(t) = [1 - \exp(-(\text{FOI}(t) + \mu)\Delta t)] S(t - \Delta t) \quad (\text{S85})$$

$$N_{SI}(t) = \frac{\text{FOI}(t)\Delta S(t)}{\text{FOI}(t) + \mu} \quad (\text{S86})$$

$$\Delta I(t) = [1 - \exp(-(\gamma + \mu)\Delta t)] I(t - \Delta t) \quad (\text{S87})$$

$$N_{IR}(t) = \frac{\gamma \Delta I(t)}{\gamma + \mu} \quad (\text{S88})$$

$$\Delta R(t) = [1 - \exp(-(\nu + \mu)\Delta t)] R(t - \Delta t) \quad (\text{S89})$$

$$N_{RS}(t) = \frac{\nu \Delta R(t)}{\nu + \mu} \quad (\text{S90})$$

$$S(t) = S(t - \Delta t) + \mu S - \Delta S(t) + N_{RS}(t) \quad (\text{S91})$$

$$I(t) = I(t - \Delta t) - \Delta I(t) + N_{SI}(t) \quad (\text{S92})$$

$$R(t) = R(t - \Delta t) - \Delta R(t) + N_{IR}(t) \quad (\text{S93})$$

720 where we include an extra term  $\omega$  to account for importation. Although actual  
721 simulations did not include any importation, we had found that including this term  
722 generally helped with model convergence in previous analyses [4]. The transmission  
723 rate was divided into a seasonal term  $\beta_{\text{seas}}(t)$  (repeated every year) and intervention  
724 term  $\alpha(t)$ , which were estimated jointly:

$$\beta(t) = \beta_{\text{seas}}(t)\alpha(t), \quad (\text{S94})$$

725 where  $\alpha < 1$  corresponds to reduction in transmission due to intervention effects. To  
726 constrain the smoothness of  $\beta_{\text{seas}}(t)$ , we imposed cyclic, random-walk priors:

$$\beta_{\text{seas}}(t) \sim \text{Normal}(\beta_{\text{seas}}(t - 1), \sigma) \quad t = 2 \dots 52 \quad (\text{S95})$$

$$\beta_{\text{seas}}(1) \sim \text{Normal}(\beta_{\text{seas}}(52), \sigma) \quad (\text{S96})$$

$$\sigma \sim \text{Half-Normal}(0, 1) \quad (\text{S97})$$

727 We fixed  $\alpha(t) = 1$  for all  $t < 2020$  and estimate  $\alpha$  assuming a normal prior:

$$\alpha \sim \text{Normal}(1, 0.25). \quad (\text{S98})$$

728 We assumed weakly informative priors on  $\omega$  and  $\nu$ :

$$\omega \sim \text{Half-Normal}(0, 200) \quad (\text{S99})$$

$$\nu \sim \text{Normal}(104, 26) \quad (\text{S100})$$

729 We assumed that the true birth/death rates, population sizes, and recovery rates  
730 are known. We note, however, that assuming  $\gamma = 1/\text{week}$  actually corresponds to  
731 a mean simulated infectious period of 1.6 weeks due to a time discretization, which  
732 is much longer than the true value; this approximation allows us to test whether we  
733 can still robustly estimate the intrinsic resilience given parameter mis-specification.  
734 Initial conditions were estimated with following priors:

$$S(0) = Ns(0) \quad (\text{S101})$$

$$I(0) = Ni(0) \quad (\text{S102})$$

$$s(0) \sim \text{Uniform}(0, 1) \quad (\text{S103})$$

$$i(0) \sim \text{Half-Normal}(0, 0.001) \quad (\text{S104})$$

735 Finally, the observation model was specified as follows:

$$\text{Cases}(t) \sim \text{Negative-Binomial}(\rho N_{SI}(t), \phi) \quad (\text{S105})$$

$$\rho \sim \text{Half-Normal}(0, 0.02) \quad (\text{S106})$$

$$\phi \sim \text{Half-Normal}(0, 10) \quad (\text{S107})$$

736 where  $\rho$  represents the reporting probability and  $\phi$  represents the negative binomial  
737 overdispersion parameter.

738 The model was fitted to four separate time series: (1) incidence time series from  
739 the SIRS model, (2) incidence time series for strain 1 from the two-strain model,  
740 (3) incidence time series for strain 2 from the two-strain model, and (4) combined  
741 incidence time series for strains 1 and 2 from the two-strain model. The model was  
742 fitted using rstan [45, 46]. The resulting posterior distribution was used to calculate  
743 the intrinsic resilience of the seasonally unforced system with the same parameters;  
744 eigenvalues of the discrete-time SIR model were computed by numerically finding  
745 the equilibrium and calculating the Jacobian matrix.

## 746 **Validations for window-selection criteria**

747 We used stochastic SIRS simulations to identify optimal parameters for the window-  
748 selection criteria that we used for the linear regression for estimating empirical re-  
749 silience. For each simulation, we began by generating a random perturbation  $\alpha(t)$   
750 from a random set of parameters. First, we drew the duration of perturbation  $\tau_{\text{np}}^i$

751 from a uniform distribution between 1 and 2 years. Then, we drew independent  
 752 normal variables  $z_i$  of length  $\lfloor 364\tau_{\text{np}} \rfloor$  with a standard deviation of 0.02 and took a  
 753 reverse cumulative sum to obtain a realistic shape for the perturbation:

$$x_n = 1 + \sum_{i=n}^{\lfloor 364\tau_{\text{np}} \rfloor} z_i, \quad n = 1, \dots, \lfloor 364\tau_{\text{np}} \rfloor. \quad (\text{S108})$$

754 In contrast to simple perturbations that assume a constant reduction in transmission,  
 755 this approach allows us to model transmission reduction that varies over time  
 756 smoothly. We repeated this random generation process until less than 10% of  $x_n$   
 757 exceeds 1—this was done to ensure the perturbation term  $\alpha(t)$  stays below 1 (and  
 758 therefore reduce transmission) for the most part. Then, we set any values that are  
 759 above 1 or below 0 to 1 and 0, respectively. Then, we randomly drew the minimum  
 760 transmission during perturbation  $\alpha_{\min}$  from a uniform distribution between 0.5 and  
 761 0.7 and scale  $x_n$  to have a minimum of  $\alpha_{\min}$ :

$$x_{\text{scale},n} = \alpha_{\min} + (1 - \alpha_{\min}) \times \frac{x_n - \min x_n}{1 - \min x_n}. \quad (\text{S109})$$

762 This allowed us to simulate a realistically shaped perturbation:

$$\alpha(t) = \begin{cases} 1 & t < 2020 \\ x_{\text{scale},364(t-2020)} & 2020 \leq t < 2020 + \tau_{\text{np}} \\ 1 & \tau_{\text{np}} \leq t \end{cases} \quad (\text{S110})$$

763 Given this perturbation function, we draw  $\mathcal{R}_0$  from a uniform distribution between  
 764 1.5 and 4 and the mean duration of immunity  $1/\delta$  from a uniform distribution be-  
 765 tween 1 and 4. Then, we simulate the stochastic SIRS model from  $S(0) = 10^8/\mathcal{R}_0$   
 766 and  $I(0) = 100$  from 1990 to 2025 and truncate the time series to 2014–2025; if the  
 767 epidemic becomes extinct before the end of simulation, we discard that simulation  
 768 and start over from the perturbation generation step.

769 For each epidemic simulation, we computed the empirical resilience by varying  
 770 the threshold  $R$  for the nearest neighbor approach from 4 to 14 with increments of  
 771 2, the number of divisions  $K$  for the window selection between 8 and 25, and the  
 772 truncation threshold  $a$  for the window selection between 1 to 3; this was done for all  
 773 possible combinations of  $R$ ,  $K$ , and  $a$ . We also compared this with the naive approach  
 774 that uses the entire distance-from-attractor time series, starting from the maximum  
 775 distance to the end of the time series. We repeated this procedure 500 times and  
 776 quantified the correlation between empirical and intrinsic resilience estimates across  
 777 two approaches.

<sup>778</sup> **Supplementary Figures**

779 **References**

- 780 [1] Rachel E Baker, Sang Woo Park, Wenchang Yang, Gabriel A Vecchi, C Jessica E  
781 Metcalf, and Bryan T Grenfell. The impact of COVID-19 nonpharmaceutical  
782 interventions on the future dynamics of endemic infections. *Proceedings of the*  
783 *National Academy of Sciences*, 117(48):30547–30553, 2020.
- 784 [2] Gabriela B Gomez, Cedric Mahé, and Sandra S Chaves. Uncertain effects of the  
785 pandemic on respiratory viruses. *Science*, 372(6546):1043–1044, 2021.
- 786 [3] Mihaly Koltai, Fabienne Krauer, David Hodgson, Edwin van Leeuwen, Marina  
787 Treskova-Schwarzbach, Mark Jit, and Stefan Flasche. Determinants of RSV  
788 epidemiology following suppression through pandemic contact restrictions. *Epi-*  
789 *demics*, 40:100614, 2022.
- 790 [4] Sang Woo Park, Brooklyn Noble, Emily Howerton, Bjarke F Nielsen, Sarah  
791 Lentz, Lilliam Ambroggio, Samuel Dominguez, Kevin Messacar, and Bryan T  
792 Grenfell. Predicting the impact of non-pharmaceutical interventions against  
793 COVID-19 on *Mycoplasma pneumoniae* in the United States. *Epidemics*,  
794 49:100808, 2024.
- 795 [5] Amanda C Perofsky, Chelsea L Hansen, Roy Burstein, Shanda Boyle, Robin  
796 Prentice, Cooper Marshall, David Reinhart, Ben Capodanno, Melissa Truong,  
797 Kristen Schwabe-Fry, et al. Impacts of human mobility on the citywide trans-  
798 mission dynamics of 18 respiratory viruses in pre-and post-COVID-19 pandemic  
799 years. *Nature communications*, 15(1):4164, 2024.
- 800 [6] Eric J Chow, Timothy M Uyeki, and Helen Y Chu. The effects of the COVID-19  
801 pandemic on community respiratory virus activity. *Nature Reviews Microbiol-*  
802 *ogy*, 21(3):195–210, 2023.
- 803 [7] Stephen M Kissler, Christine Tedijanto, Edward Goldstein, Yonatan H Grad,  
804 and Marc Lipsitch. Projecting the transmission dynamics of SARS-CoV-2  
805 through the postpandemic period. *Science*, 368(6493):860–868, 2020.
- 806 [8] Rachel E Baker, Chadi M Saad-Roy, Sang Woo Park, Jeremy Farrar, C Jessica E  
807 Metcalf, and Bryan T Grenfell. Long-term benefits of nonpharmaceutical inter-  
808 ventions for endemic infections are shaped by respiratory pathogen dynamics.  
809 *Proceedings of the National Academy of Sciences*, 119(49):e2208895119, 2022.
- 810 [9] Maaike C Swets, Clark D Russell, Ewen M Harrison, Annemarie B Docherty,  
811 Nazir Lone, Michelle Girvan, Hayley E Hardwick, Leonardus G Visser, Pe-  
812 ter JM Openshaw, Geert H Groeneveld, et al. SARS-CoV-2 co-infection with  
813 influenza viruses, respiratory syncytial virus, or adenoviruses. *The Lancet*,  
814 399(10334):1463–1464, 2022.

- 815 [10] Chun-Yang Lin, Joshua Wolf, David C Brice, Yilun Sun, Macauley Locke,  
816 Sean Cherry, Ashley H Castellaw, Marie Wehenkel, Jeremy Chase Crawford,  
817 Veronika I Zarnitsyna, et al. Pre-existing humoral immunity to human common  
818 cold coronaviruses negatively impacts the protective SARS-CoV-2 antibody re-  
819 sponse. *Cell host & microbe*, 30(1):83–96, 2022.
- 820 [11] Sam M Murray, Azim M Ansari, John Frater, Paul Klenerman, Susanna  
821 Dunachie, Eleanor Barnes, and Ane Ogbe. The impact of pre-existing cross-  
822 reactive immunity on SARS-CoV-2 infection and vaccine responses. *Nature*  
823 *Reviews Immunology*, 23(5):304–316, 2023.
- 824 [12] John-Sebastian Eden, Chisha Sikazwe, Ruopeng Xie, Yi-Mo Deng, Sheena G  
825 Sullivan, Alice Michie, Avram Levy, Elena Cutmore, Christopher C Blyth,  
826 Philip N Britton, et al. Off-season RSV epidemics in Australia after easing  
827 of COVID-19 restrictions. *Nature communications*, 13(1):2884, 2022.
- 828 [13] Stuart L Pimm. The structure of food webs. *Theoretical population biology*,  
829 16(2):144–158, 1979.
- 830 [14] Michael G Neubert and Hal Caswell. Alternatives to resilience for measuring  
831 the responses of ecological systems to perturbations. *Ecology*, 78(3):653–665,  
832 1997.
- 833 [15] Lance H Gunderson. Ecological resilience—in theory and application. *Annual*  
834 *review of ecology and systematics*, 31(1):425–439, 2000.
- 835 [16] Vasilis Dakos and Sonia Kéfi. Ecological resilience: what to measure and how.  
836 *Environmental Research Letters*, 17(4):043003, 2022.
- 837 [17] Floris Takens. Detecting strange attractors in turbulence. In *Dynamical Sys-*  
838 *tems and Turbulence, Warwick 1980: proceedings of a symposium held at the*  
839 *University of Warwick 1979/80*, pages 366–381. Springer, 2006.
- 840 [18] Jonathan Dushoff, Joshua B Plotkin, Simon A Levin, and David JD Earn.  
841 Dynamical resonance can account for seasonality of influenza epidemics. *Pro-*  
842 , 101(48):16915–16916, 2004.
- 843 [19] Alan Hastings, Carole L Hom, Stephen Ellner, Peter Turchin, and H Charles J  
844 Godfray. Chaos in ecology: is mother nature a strange attractor? *Annual review*  
845 *of ecology and systematics*, pages 1–33, 1993.
- 846 [20] Alan Hastings, Karen C Abbott, Kim Cuddington, Tessa Francis, Gabriel Gell-  
847 ner, Ying-Cheng Lai, Andrew Morozov, Sergei Petrovskii, Katherine Scran-  
848 ton, and Mary Lou Zeeman. Transient phenomena in ecology. *Science*,  
849 361(6406):eaat6412, 2018.

- 850 [21] Matthew B Kennel, Reggie Brown, and Henry DI Abarbanel. Determining  
851 embedding dimension for phase-space reconstruction using a geometrical con-  
852 struction. *Physical review A*, 45(6):3403, 1992.
- 853 [22] Eugene Tan, Shannon Algar, Débora Corrêa, Michael Small, Thomas Stemler,  
854 and David Walker. Selecting embedding delays: An overview of embedding  
855 techniques and a new method using persistent homology. *Chaos: An Interdis-*  
856 *ciplinary Journal of Nonlinear Science*, 33(3), 2023.
- 857 [23] Bjarke Frost Nielsen, Sang Woo Park, Emily Howerton, Olivia Frost Lorentzen,  
858 Mogens H Jensen, and Bryan T Grenfell. Complex multiannual cycles of My-  
859 coplasma pneumoniae: persistence and the role of stochasticity. *arXiv*, 2025.
- 860 [24] Samantha Bosis, Susanna Esposito, HGM Niesters, GV Zuccotti, G Marseglia,  
861 Marcello Lanari, Giovanna Zuin, C Pelucchi, ADME Osterhaus, and Nicola  
862 Principi. Role of respiratory pathogens in infants hospitalized for a first episode  
863 of wheezing and their impact on recurrences. *Clinical microbiology and infection*,  
864 14(7):677–684, 2008.
- 865 [25] Miguel L O’Ryan, Yalda Lucero, Valeria Prado, María Elena Santolaya, Marcela  
866 Rabello, Yanahara Solis, Daniela Berriós, Miguel A O’Ryan-Soriano, Hector  
867 Cortés, and Nora Mamani. Symptomatic and asymptomatic rotavirus and  
868 norovirus infections during infancy in a Chilean birth cohort. *The Pediatric  
869 infectious disease journal*, 28(10):879–884, 2009.
- 870 [26] Virginia E Pitzer, Cécile Viboud, Vladimir J Alonso, Tanya Wilcox, C Jessica  
871 Metcalf, Claudia A Steiner, Amber K Haynes, and Bryan T Grenfell. Environmental  
872 drivers of the spatiotemporal dynamics of respiratory syncytial virus in  
873 the United States. *PLoS pathogens*, 11(1):e1004591, 2015.
- 874 [27] Arthur WD Edridge, Joanna Kaczorowska, Alexis CR Hoste, Margreet Bakker,  
875 Michelle Klein, Katherine Loens, Maarten F Jebbink, Amy Matser, Cormac M  
876 Kinsella, Paloma Rueda, et al. Seasonal coronavirus protective immunity is  
877 short-lasting. *Nature medicine*, 26(11):1691–1693, 2020.
- 878 [28] Jennifer M Radin, Anthony W Hawksworth, Peter E Kammerer, Melinda Bal-  
879 ansay, Rema Raman, Suzanne P Lindsay, and Gary T Brice. Epidemiology  
880 of pathogen-specific respiratory infections among three US populations. *PLoS  
881 One*, 9(12):e114871, 2014.
- 882 [29] Guojian Lv, Limei Shi, Yi Liu, Xuecheng Sun, and Kai Mu. Epidemiological  
883 characteristics of common respiratory pathogens in children. *Scientific Reports*,  
884 14(1):16299, 2024.
- 885 [30] Saverio Caini, Adam Meijer, Marta C Nunes, Laetitia Henaff, Malaika Zounon,  
886 Bronke Boudewijns, Marco Del Riccio, and John Paget. Probable extinction of

- 887 influenza b/yamagata and its public health implications: a systematic literature  
888 review and assessment of global surveillance databases. *The Lancet Microbe*,  
889 2024.
- 890 [31] Zhiyuan Chen, Joseph L-H Tsui, Bernardo Gutierrez, Simon Busch Moreno,  
891 Louis du Plessis, Xiaowei Deng, Jun Cai, Sumali Bajaj, Marc A Suchard,  
892 Oliver G Pybus, et al. COVID-19 pandemic interventions reshaped the global  
893 dispersal of seasonal influenza viruses. *Science*, 386(6722):eadq3003, 2024.
- 894 [32] Bryan T Grenfell, Ottar N Bjørnstad, and Bärbel F Finkenstädt. Dynamics of  
895 measles epidemics: scaling noise, determinism, and predictability with the TSIR  
896 model. *Ecological monographs*, 72(2):185–202, 2002.
- 897 [33] Samit Bhattacharyya, Per H Gesteland, Kent Korgenski, Ottar N Bjørnstad,  
898 and Frederick R Adler. Cross-immunity between strains explains the dynamical  
899 pattern of paramyxoviruses. *Proceedings of the National Academy of Sciences*,  
900 112(43):13396–13400, 2015.
- 901 [34] Katharine R Dean, Fabienne Krauer, Lars Walløe, Ole Christian Lingjærde, Bar-  
902 bara Bramanti, Nils Chr Stenseth, and Boris V Schmid. Human ectoparasites  
903 and the spread of plague in Europe during the Second Pandemic. *Proceedings  
904 of the National Academy of Sciences*, 115(6):1304–1309, 2018.
- 905 [35] Margarita Pons-Salort and Nicholas C Grassly. Serotype-specific immunity  
906 explains the incidence of diseases caused by human enteroviruses. *Science*,  
907 361(6404):800–803, 2018.
- 908 [36] Sarah Cobey and Edward B Baskerville. Limits to causal inference with state-  
909 space reconstruction for infectious disease. *PLoS one*, 11(12):e0169050, 2016.
- 910 [37] Public Health Agency of Canada. Respiratory virus detections in  
911 Canada. 2024. <https://www.canada.ca/en/public-health/services/surveillance/respiratory-virus-detections-canada.html>. Accessed Sep  
912 4, 2024.
- 913 [38] Centre for Health Protection. Detection of pathogens from respiratory spec-  
914 imens. 2024. <https://www.chp.gov.hk/en/statistics/data/10/641/642/2274.html>. Accessed Nov 20, 2024.
- 915 [39] Centre for Health Protection. Detection of gastroenteritis viruses from faecal  
916 specimens. 2024. <https://www.chp.gov.hk/en/statistics/data/10/641/717/3957.html>. Accessed Nov 20, 2024.
- 917 [40] Korea Disease Control and Prevention Agency. Acute respiratory infection,  
918 Sentinel surveillance infectious diseases. 2024. <https://dportal.kdca.go.kr/pot/is/st/ari.do>. Accessed Nov 20, 2024.

- 923 [41] Edward Goldstein, Sarah Cobey, Saki Takahashi, Joel C Miller, and Marc Lipsitch. Predicting the epidemic sizes of influenza A/H1N1, A/H3N2, and B: a  
924 statistical method. *PLoS medicine*, 8(7):e1001051, 2011.
- 925
- 926 [42] Karline Soetaert, Thomas Petzoldt, and R Woodrow Setzer. Solving differential  
927 equations in R: package deSolve. *Journal of statistical software*, 33:1–25, 2010.
- 928 [43] R Core Team. *R: A Language and Environment for Statistical Computing*. R  
929 Foundation for Statistical Computing, Vienna, Austria, 2023.
- 930 [44] Sang Woo Park, Inga Holmdahl, Emily Howerton, Wenchang Yang, Rachel E  
931 Baker, Gabriel A Vecchi, Sarah Cobey, C Jessica E Metcalf, and Bryan T Grenfell.  
932 Interplay between climate, childhood mixing, and population-level suscep-  
933 tibility explains a sudden shift in RSV seasonality in Japan. *medRxiv*, pages  
934 2025–03, 2025.
- 935 [45] Bob Carpenter, Andrew Gelman, Matthew D Hoffman, Daniel Lee, Ben  
936 Goodrich, Michael Betancourt, Marcus A Brubaker, Jiqiang Guo, Peter Li,  
937 and Allen Riddell. Stan: A probabilistic programming language. *Journal of  
938 statistical software*, 76, 2017.
- 939 [46] Stan Development Team. RStan: the R interface to Stan, 2024. R package  
940 version 2.32.6.

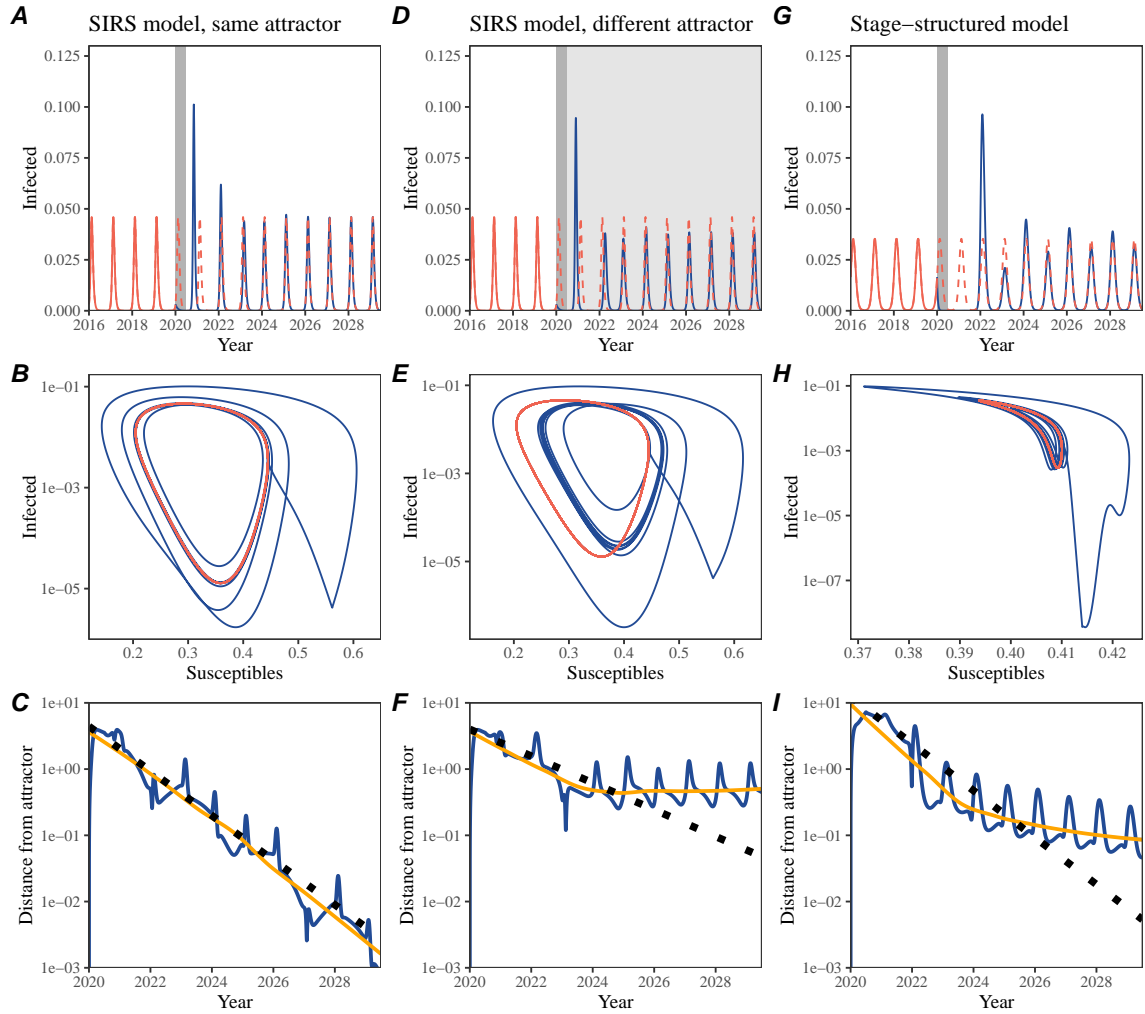


**Figure 2: A simple method to measure pathogen resilience following pandemic perturbations across different scenarios.** (A, D, G) Simulated epidemic trajectories across various models. Red and blue solid lines represent epidemic dynamics before and after pandemic perturbations are introduced, respectively. Red dashed lines represent counterfactual epidemic dynamics in the absence of perturbations. Gray regions indicate the duration of perturbations with the dark gray region representing a 50% transmission reduction and the light gray region representing a 10% transmission reduction. (B, E, H) Phase plane representation of the time series in panels A, D, and G alongside the corresponding susceptible host dynamics. Red and blue solid lines represent epidemic trajectories on an SI phase plane before and after perturbations are introduced, respectively. (C, F, I) Changes in distance from the attractor over time on a log scale. Blue lines represent the distance from the attractor. Orange lines represent the locally estimated scatterplot smoothing (LOESS) fits to the logged distance from the attractor. Dotted lines show the intrinsic resilience of the seasonally unforced system.

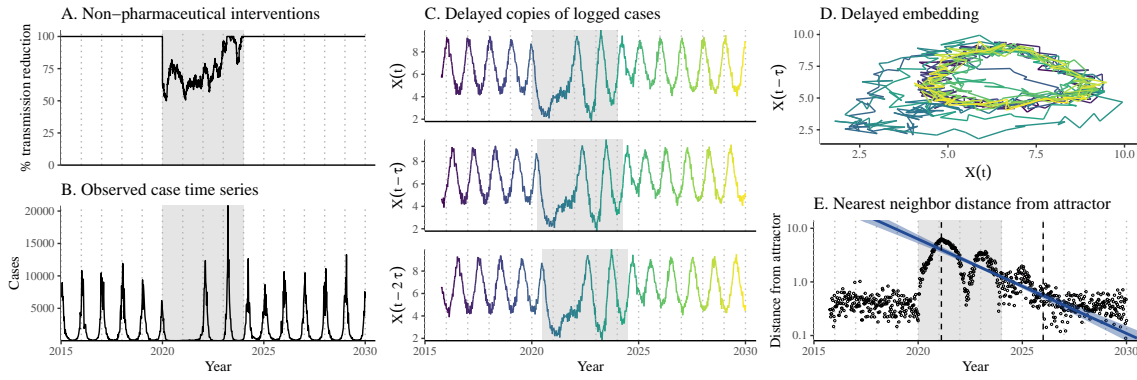


**Figure 3: A schematic diagram explaining the inference of pathogen resilience from synthetic data.** (A) A realistic example of simulated pandemic perturbations, represented by a relative reduction in transmission. (B) The impact of the synthetic pandemic perturbation on epidemic dynamics simulated using a SIRS model with demographic stochasticity. (C) Generating delayed copies of the logged time series allows us to obtain an embedding. (D) Two dimensional representation of an embedding. (E) Delayed embedding allows us to calculate the nearest neighbor distance from the empirical attractor, which is determined based on the pre-pandemic time series. Blue lines and dashed regions represent the linear regression fit and the associated 95% confidence interval. This distance time series can be used to infer pathogen resilience after choosing an appropriate window for linear regression. For illustration purposes, an arbitrary fitting window was chosen.

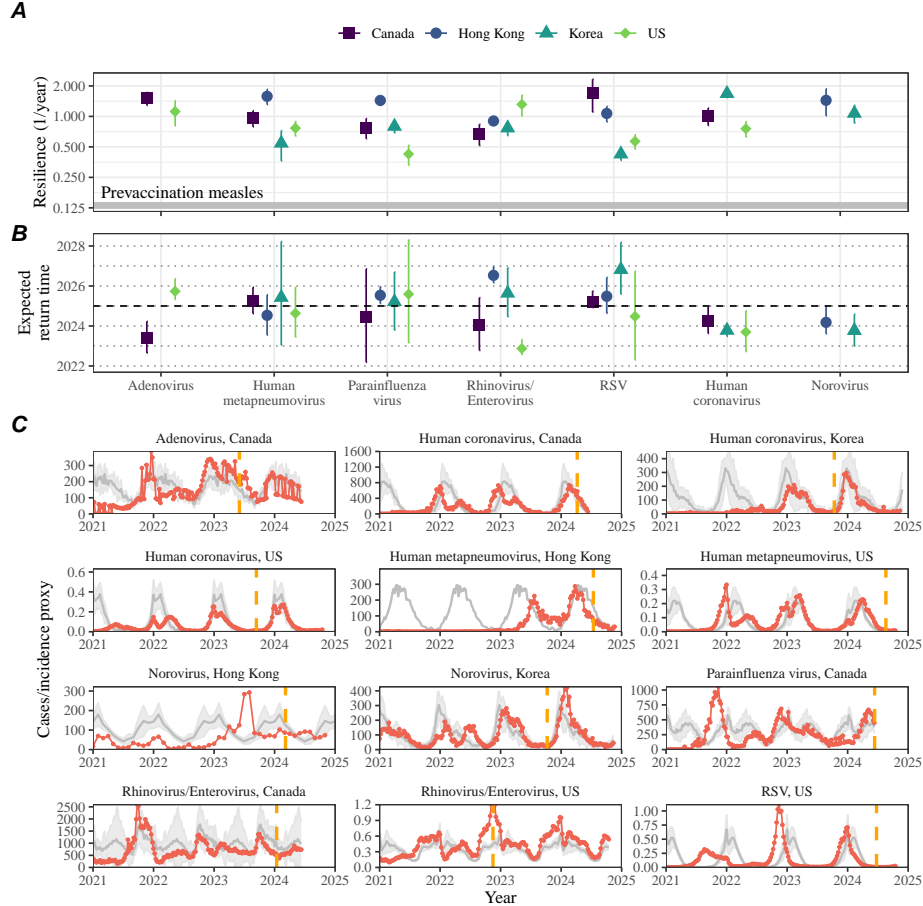


**Figure 4: Summary of resilience estimates and predictions for return time.** (A) Estimated pathogen resilience. The gray horizontal line represents the intrinsic resilience of pre-vaccination measles dynamics. (B) Predicted timing of when each pathogen will return to their pre-pandemic cycles. The dashed line in panel B indicates the end of 2024. Error bars represent 95% confidence intervals. (C) Observed dynamics for pathogen that are predicted to have returned before the end of 2024. Red points and lines represent data before 2020. Gray lines and shaded regions represent the mean seasonal patterns and corresponding 95% confidence intervals around the mean, previously shown in Figure 1. Orange vertical lines represent the predicted timing of return.

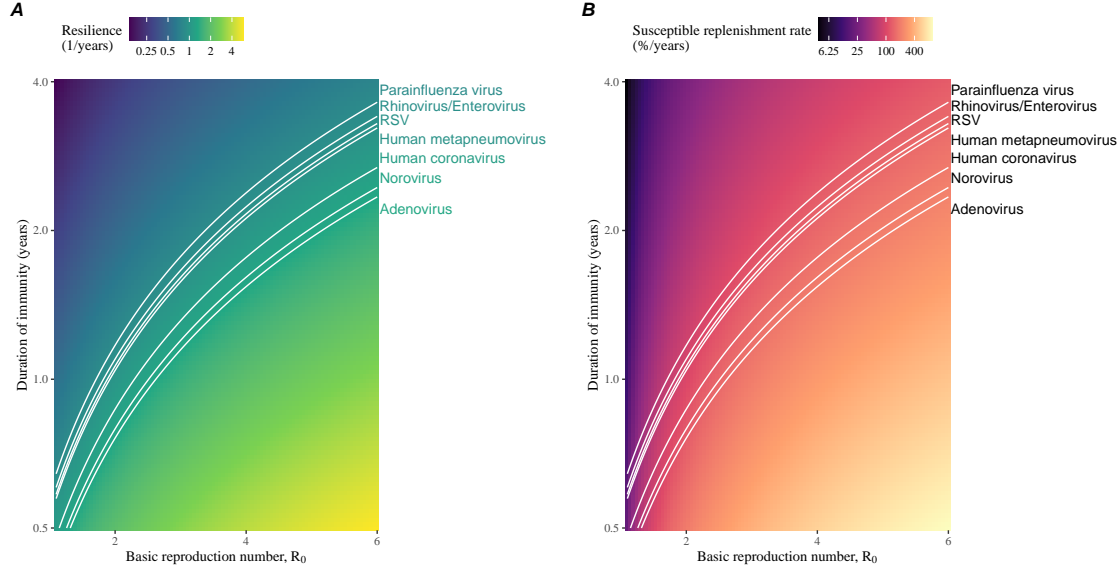


**Figure 5: Linking pathogen resilience to epidemiological parameters and susceptible host dynamics.** (A) Intrinsic resilience as a function of the basic reproduction number  $\mathcal{R}_0$  and the duration of immunity. (B) Per-capita susceptible replenishment rate as a function of the basic reproduction number  $\mathcal{R}_0$  and the duration of immunity. The standard SIRS model without seasonal forcing is used to compute intrinsic resilience and the per-capita susceptible replenishment rate. Lines correspond to a set of parameters that are consistent with mean resilience estimates for each pathogen, averaged across different countries.

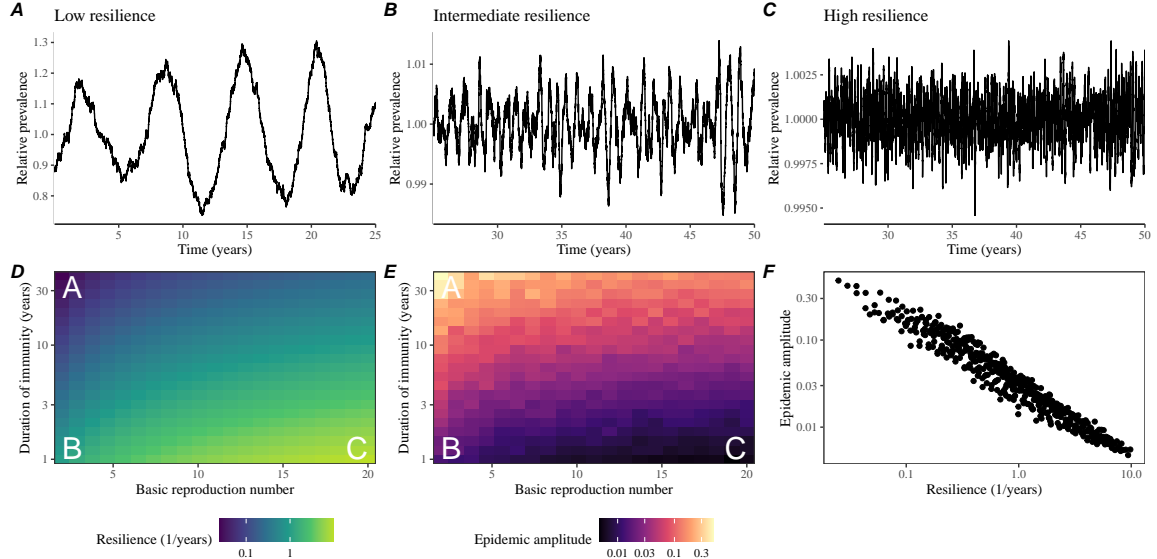


**Figure 6: Linking resilience of a host-pathogen system to its sensitivity to stochastic perturbations.** (A–C) Epidemic trajectories of a stochastic SIRS model across three different resilience values: low, intermediate, and high. The relative prevalence was calculated by dividing infection prevalence by its mean value. (D) Intrinsic resilience of a system as a function of the basic reproduction number  $\mathcal{R}_0$  and the duration of immunity. (E) Epidemic amplitude as a function of the basic reproduction number  $\mathcal{R}_0$  and the duration of immunity. The epidemic amplitude corresponds to  $(\max I - \min I)/(2\bar{I})$ , where  $\bar{I}$  represents the mean prevalence. Labels A–C in panels D and E correspond to scenarios shown in panels A–C. (F) The relationship between pathogen resilience and epidemic amplitude.

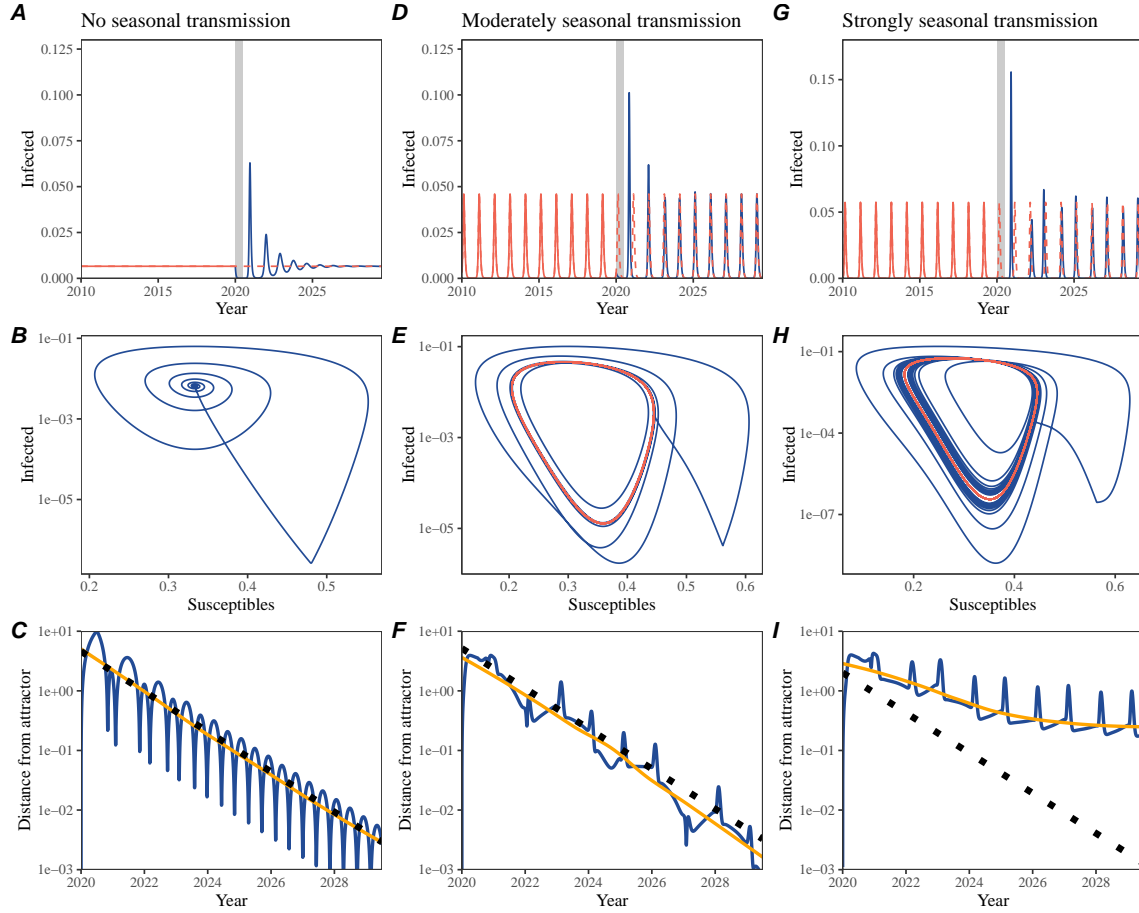


**Figure S1: Impact of seasonal transmission on pathogen resilience.** (A, D, G) Simulated epidemic trajectories using the SIRS model without seasonal forcing (A), with seasonal forcing of amplitude of 0.2 (D), and with seasonal forcing of amplitude of 0.4 (G). Red and blue solid lines represent epidemic dynamics before and after interventions are introduced, respectively. Red dashed lines represent counterfactual epidemic dynamics in the absence of interventions. Gray regions indicate the duration of interventions. (B, E, H) Phase plane representation of the time series in panels A, D, and G alongside the corresponding susceptible host dynamics. Red and blue solid lines represent epidemic trajectories on an SI phase plane before and after interventions are introduced, respectively. (C, F, I) Changes in logged distance from the attractor over time. Blue lines represent the logged distance from the attractor. Orange lines represent the locally estimated scatterplot smoothing (LOESS) fits to the logged distance from the attractor. Dotted lines show the intrinsic resilience of the seasonally unforced system.

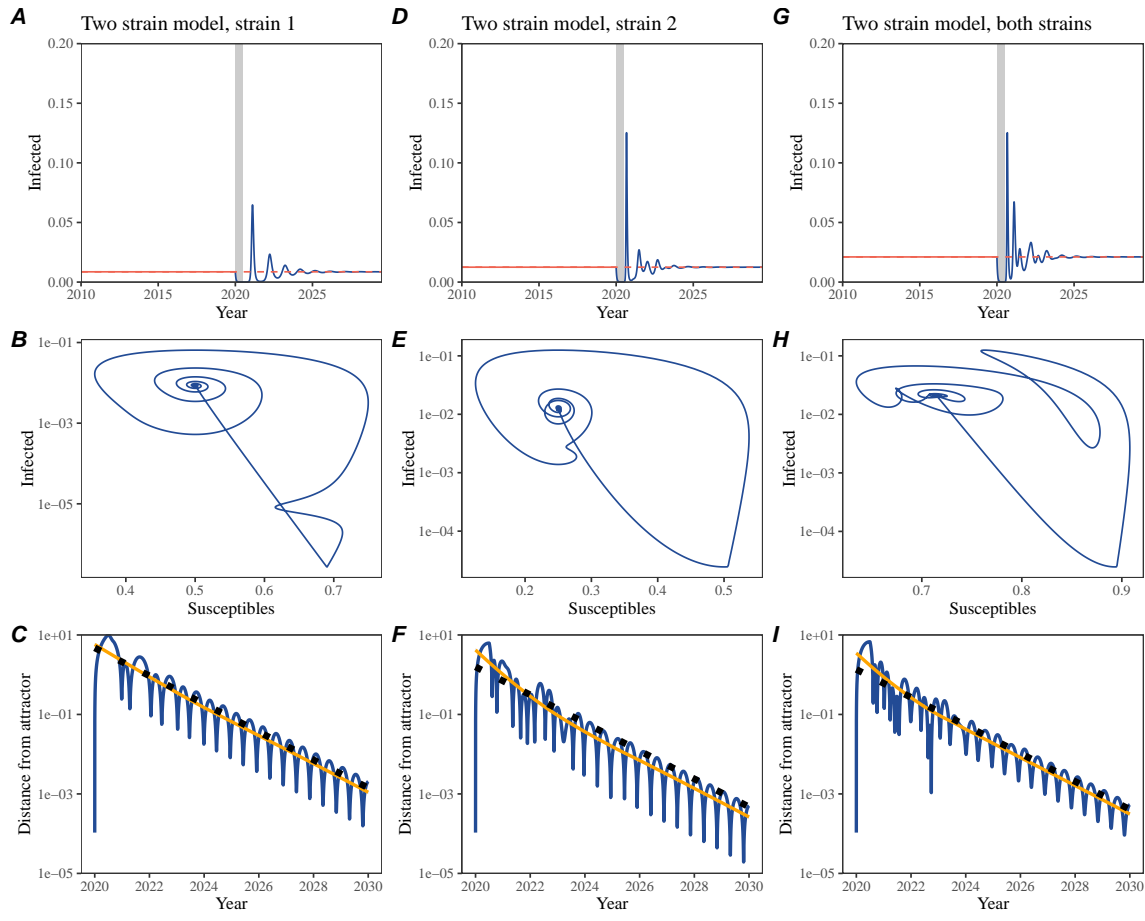


**Figure S2: A simple method to measure pathogen resilience following pandemic perturbations for a two-strain competition system without seasonal forcing.** (A, D, G) Simulated epidemic trajectories using a two-strain system without seasonal forcing. In this model, two strains compete through cross immunity. Red and blue solid lines represent epidemic dynamics before and after interventions are introduced, respectively. Red dashed lines represent counterfactual epidemic dynamics in the absence of interventions. Gray regions indicate the duration of interventions. (B, E, H) Phase plane representation of the time series in panels A, D, and G alongside the corresponding susceptible host dynamics. Blue solid lines represent epidemic trajectories on an SI phase plane before and after interventions are introduced, respectively. (C, F, I) Changes in logged distance from the attractor over time. Blue lines represent the logged distance from the attractor. Orange lines represent the locally estimated scatterplot smoothing (LOESS) fits to the logged distance from the attractor. Dotted lines show the intrinsic resilience of the seasonally unforced system.

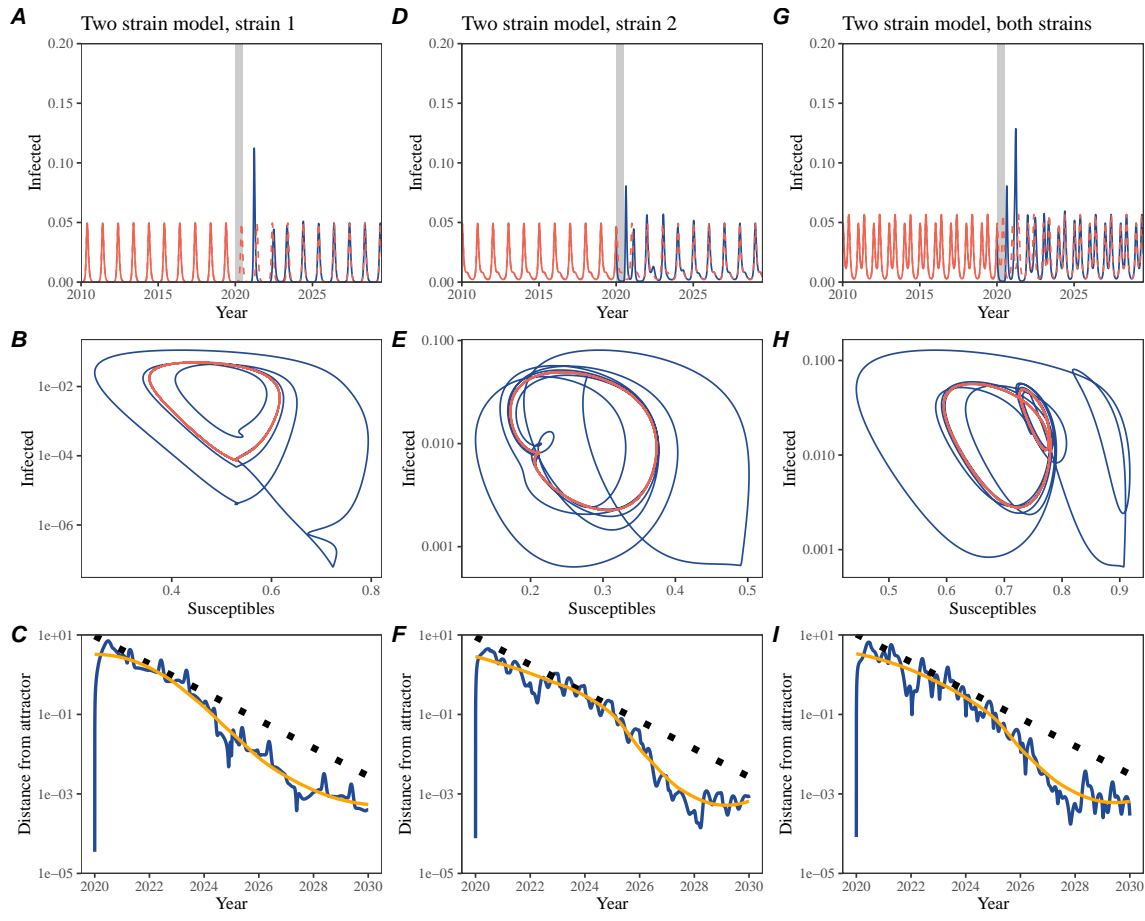


**Figure S3: A simple method to measure pathogen resilience following pandemic perturbations for a two-strain competition system with seasonal forcing.** (A, D, G) Simulated epidemic trajectories using a two-strain system with seasonal forcing (amplitude of 0.2). In this model, two strains compete through cross immunity. Red and blue solid lines represent epidemic dynamics before and after interventions are introduced, respectively. Red dashed lines represent counterfactual epidemic dynamics in the absence of interventions. Gray regions indicate the duration of interventions. (B, E, H) Phase plane representation of the time series in panels A, D, and G alongside the corresponding susceptible host dynamics. Red and blue solid lines represent epidemic trajectories on an SI phase plane before and after interventions are introduced, respectively. (C, F, I) Changes in logged distance over time. Blue lines represent the logged distance from the attractor. Orange lines represent the locally estimated scatterplot smoothing (LOESS) fits to the logged distance from the attractor. Dotted lines show the intrinsic resilience of the seasonally unforced system.

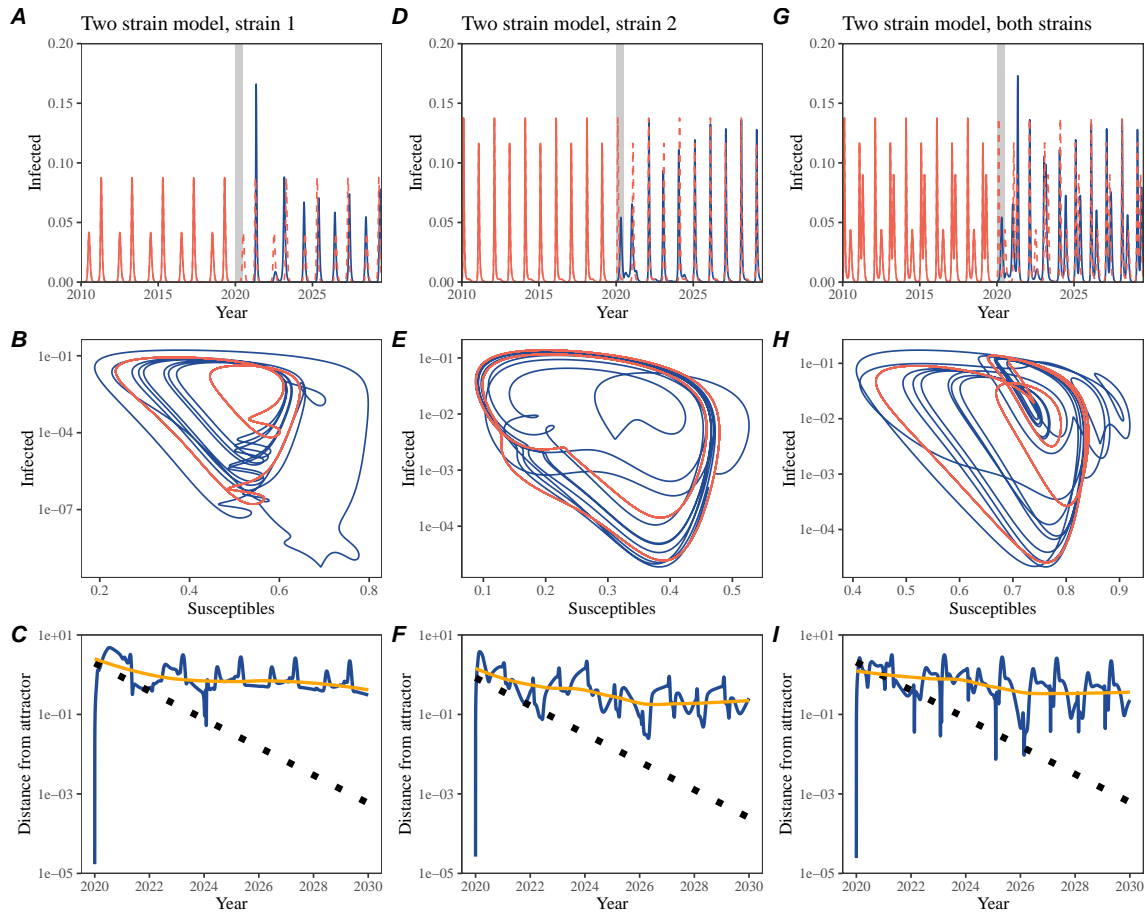


**Figure S4: A simple method to measure pathogen resilience following pandemic perturbations for a multi-strain competition system with strong seasonal forcing.** (A, D, G) Simulated epidemic trajectories using a two-strain system with seasonal forcing (amplitude of 0.2). In this model, two strains compete through cross immunity. Red and blue solid lines represent epidemic dynamics before and after interventions are introduced, respectively. Red dashed lines represent counterfactual epidemic dynamics in the absence of interventions. Gray regions indicate the duration of interventions. (B, E, H) Phase plane representation of the time series in panels A, D, and G alongside the corresponding susceptible host dynamics. Red and blue solid lines represent epidemic trajectories on an SI phase plane before and after interventions are introduced, respectively. (C, F, I) Changes in logged distance from the attractor over time. Blue lines represent the logged distance from the attractor. Orange lines represent the locally estimated scatterplot smoothing (LOESS) fits to the logged distance from the attractor. Dotted lines show the intrinsic resilience of the seasonally unforced system.

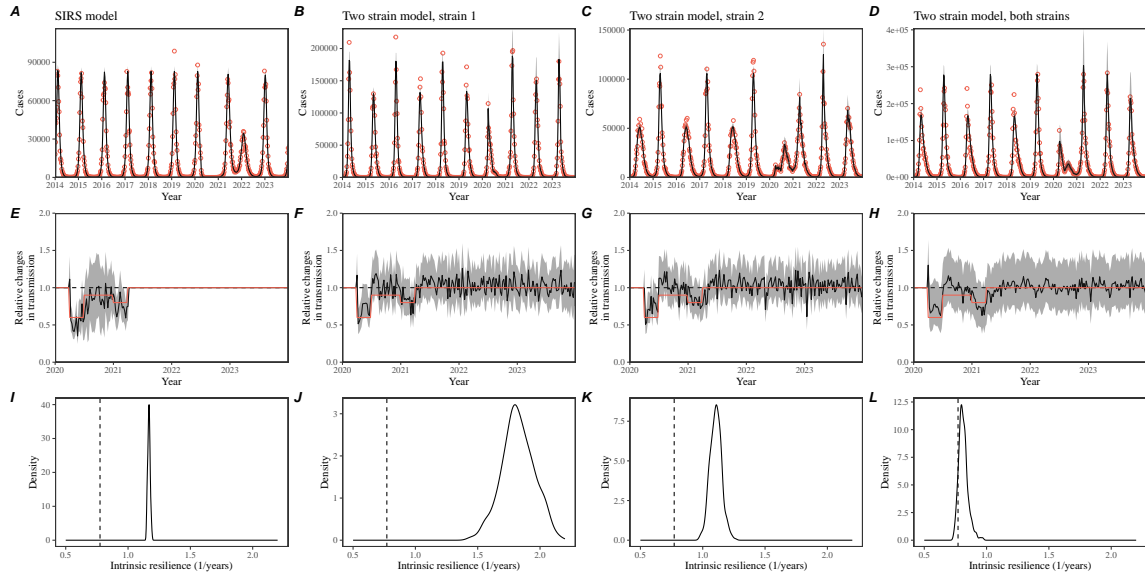


**Figure S5: Mechanistic model fits to simulated data and inferred intrinsic resilience.** We simulated discrete time, stochastic epidemic trajectories using a seasonally forced SIRS model (A,E,I) and a seasonally forced two-strain model (B–D, F–H, and J–L) and tested whether we can estimate the intrinsic resilience of the seasonally unforced versions of the model by fitting a mechanistic model (Supplementary Text). We fitted the same discrete time, one strain, deterministic SIRS model in each scenario. (A–D) Simulated case time series from corresponding models shown in the title (red) and SIRS model fits (black). (E–H) Assumed changes in transmission due to pandemic perturbations (red) and estimated time-varying relative transmission rates for the perturbation impact from the SIRS model fits (black). Solid lines and shaded regions represent fitted posterior median and 95% credible intervals. (I–L) Comparisons between the true and estimated intrinsic resilience of the seasonally unforced system. Vertical lines represent the true intrinsic resilience of the seasonally unforced system. Density plots represent the posterior distribution of the inferred intrinsic resilience of the seasonally unforced SIRS model using fitted parameters.

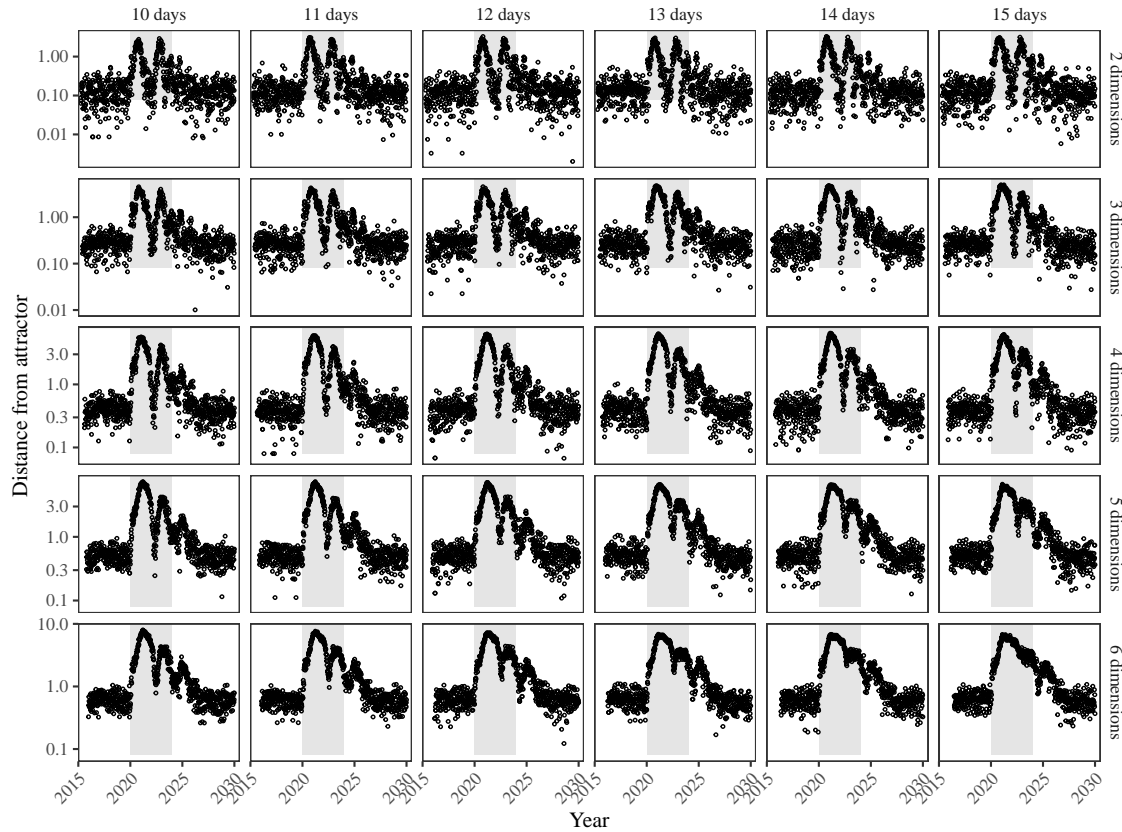


**Figure S6: Sensitivity of the distance from the attractor to choice of embedding lags and dimensions.** Sensitivity analysis for the distance-from-attractor time series shown in Figure 3E in the main text by varying the embedding lag between 10–15 days and embedding dimensions between 2–6 dimensions. The gray region represents the assumed period of pandemic perturbation.

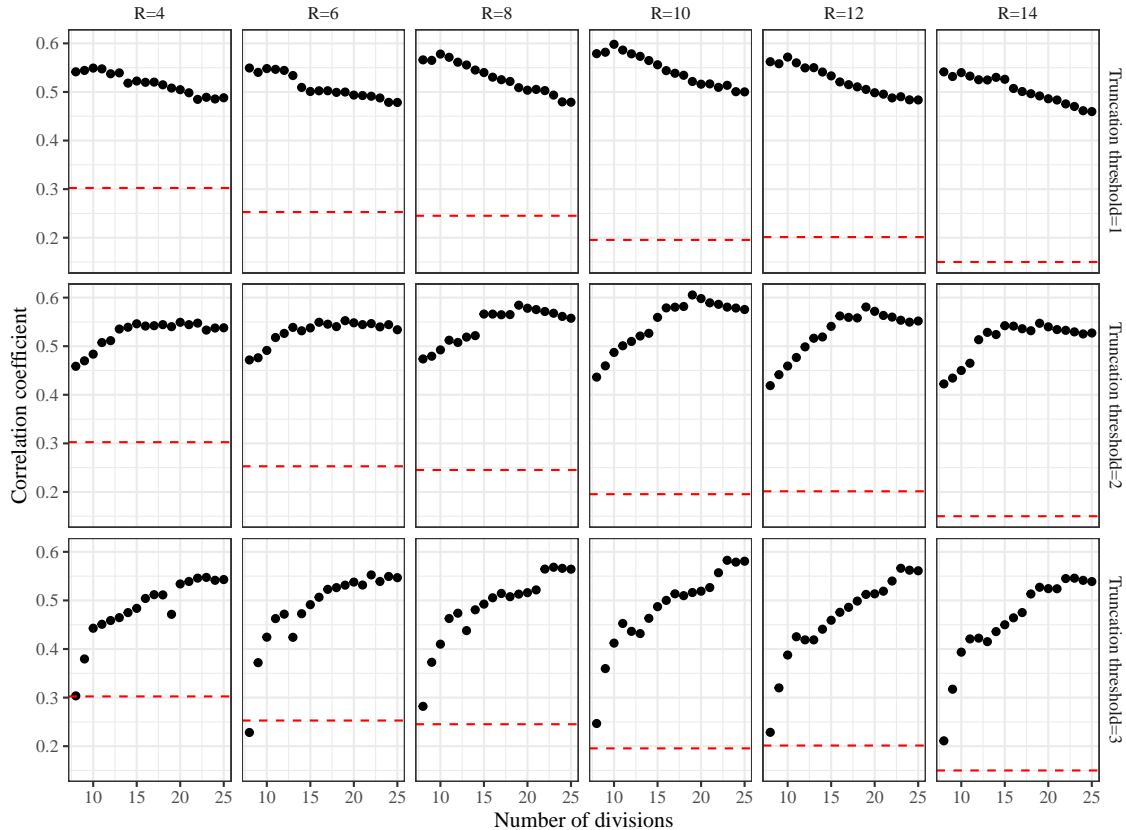


**Figure S7: Impact of fitting window selection on the estimation of empirical resilience.** We simulated 500 epidemics of a stochastic SIRS model with randomly drawn parameters and randomly generated pandemic perturbations (Supplementary Text). For each simulation, we varied the false nearest neighbor threshold  $R$  for reconstructing the empirical attractor as well as the parameters for regression window selection (i.e., the truncation threshold  $a$  and the number of divisions  $K$ ). Each point represents the resulting correlation coefficient between empirical and intrinsic resilience estimates for a given scenario. Dashed lines represent the correlation coefficient between empirical and intrinsic resilience estimates for the naive approach that fits a linear regression on a log scale, starting from the maximum distance until the end of the time series.

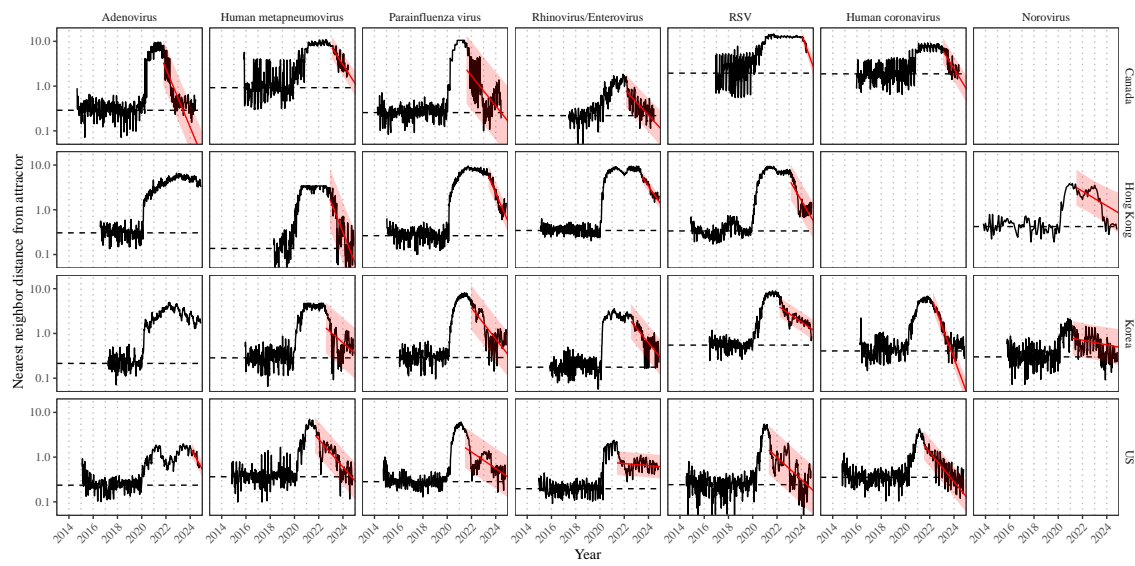


**Figure S8: Estimated time series of distance from the attractor for each pathogen and corresponding linear regression fits using automated window selection criterion across Canada, Hong Kong, Korea, and the US.** Black lines represent the estimated distance from the attractor. Red lines and shaded regions represent the linear regression fits and corresponding 95% confidence intervals. Dashed lines represent the average of the pre-pandemic nearest neighbor distances.

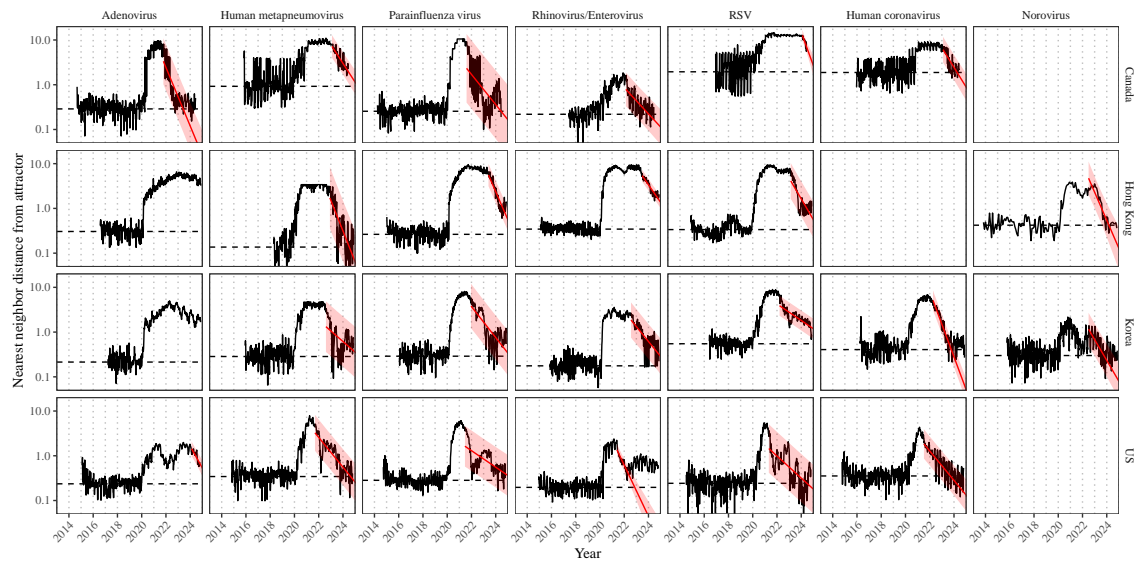


**Figure S9: Estimated time series of distance from the attractor for each pathogen and corresponding linear regression fits across Canada, Hong Kong, Korea, and the US, including ad-hoc regression window selection.** We used ad-hoc regression windows for norovirus in Hong Kong and Korea and rhinovirus/enterovirus in the US. Black lines represent the estimated distance from the attractor. Red lines and shaded regions represent the linear regression fits and corresponding 95% confidence intervals. Dashed lines represent the average of the pre-pandemic nearest neighbor distances.

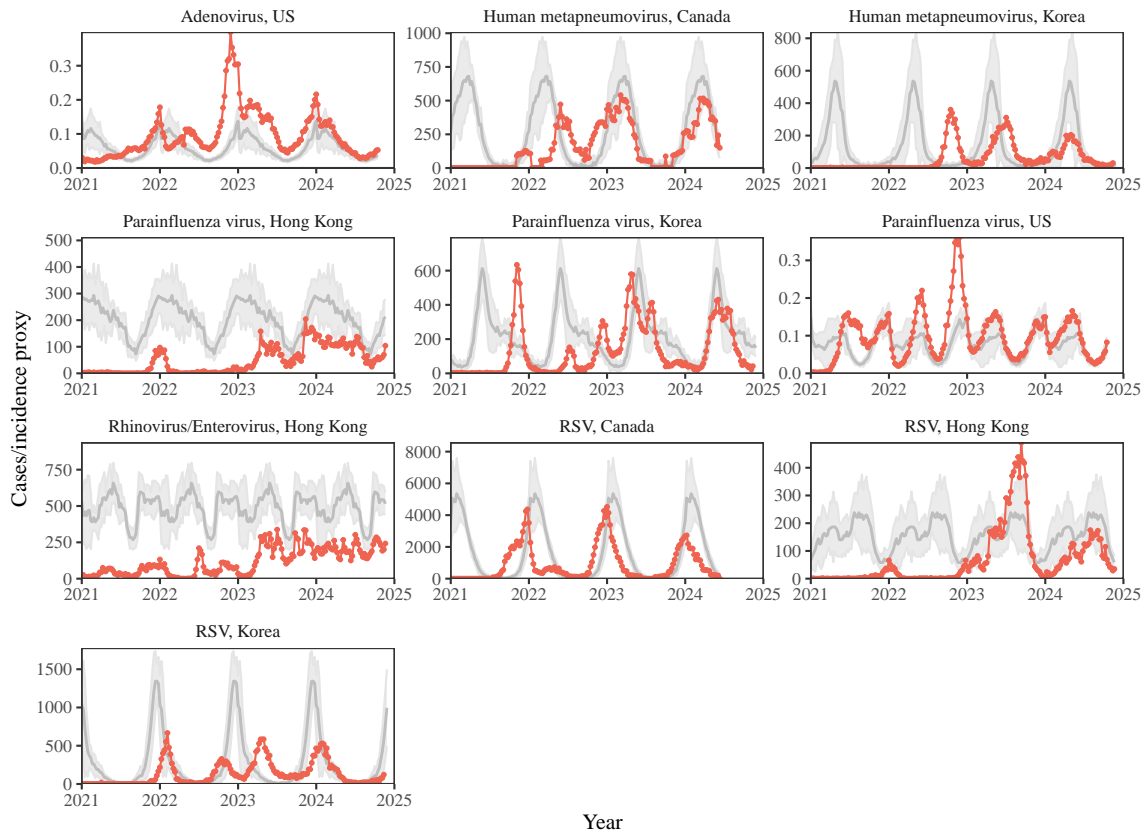


**Figure S10: Observed dynamics for pathogen that are predicted to return after the end of 2024.** Red points and lines represent data before 2020. Gray lines and shaded regions represent the mean seasonal patterns and corresponding 95% confidence intervals around the mean, previously shown in Figure 1.

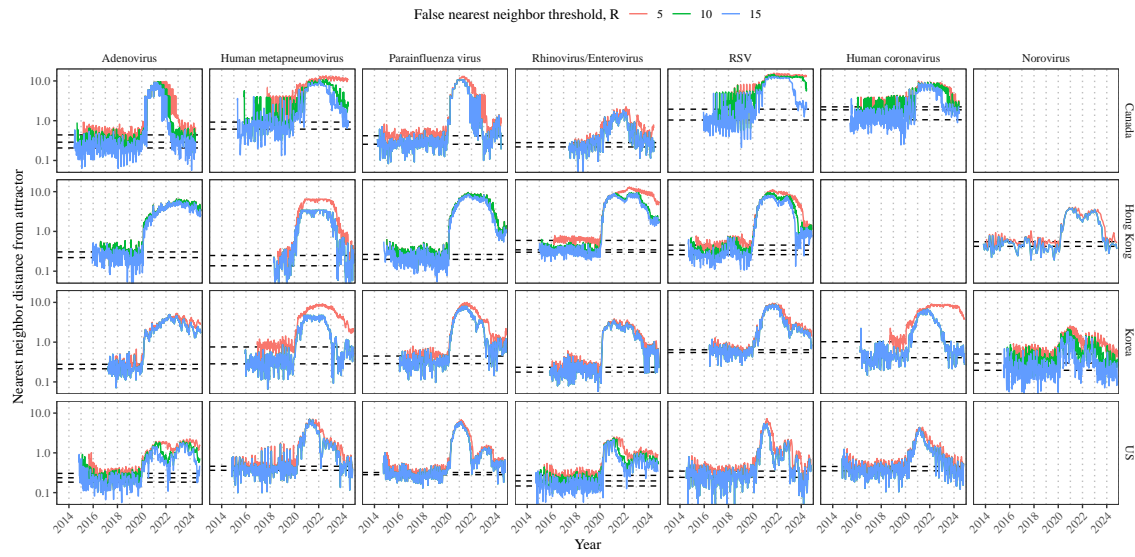


**Figure S11: Estimated time series of distance from the attractor for each pathogen across different choices about false nearest neighbor threshold values.** Using higher threshold values for the false nearest neighbor approach gives lower embedding dimensions. Colored lines represent the estimated distance from the attractor for different threshold values.

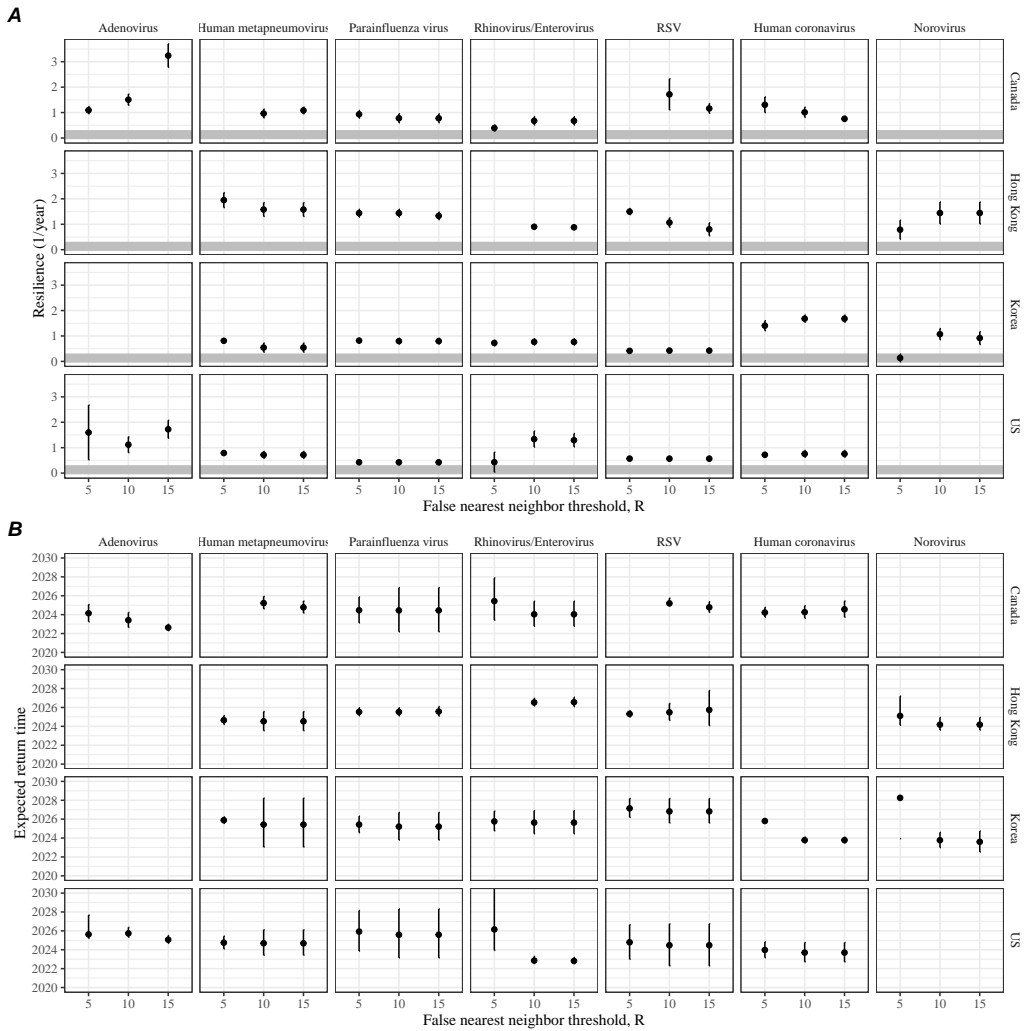


**Figure S12: Summary of resilience estimates and predictions for return time across different choices about false nearest neighbor threshold values.** The automated window selection method was used for all scenarios to estimate pathogen resilience, except for norovirus in Hong Kong and Korea and rhinovirus/enterovirus in the US. We used the same ad-hoc regression windows for norovirus in Hong Kong and Korea and rhinovirus/enterovirus in the US as we did in the main analysis. (A) Estimated pathogen resilience. The gray horizontal line represents the intrinsic resilience of pre-vaccination measles dynamics. (B) Predicted timing of when each pathogen will return to their pre-pandemic cycles. The dashed line in panel B indicates the end of 2024. Error bars represent 95% confidence intervals.

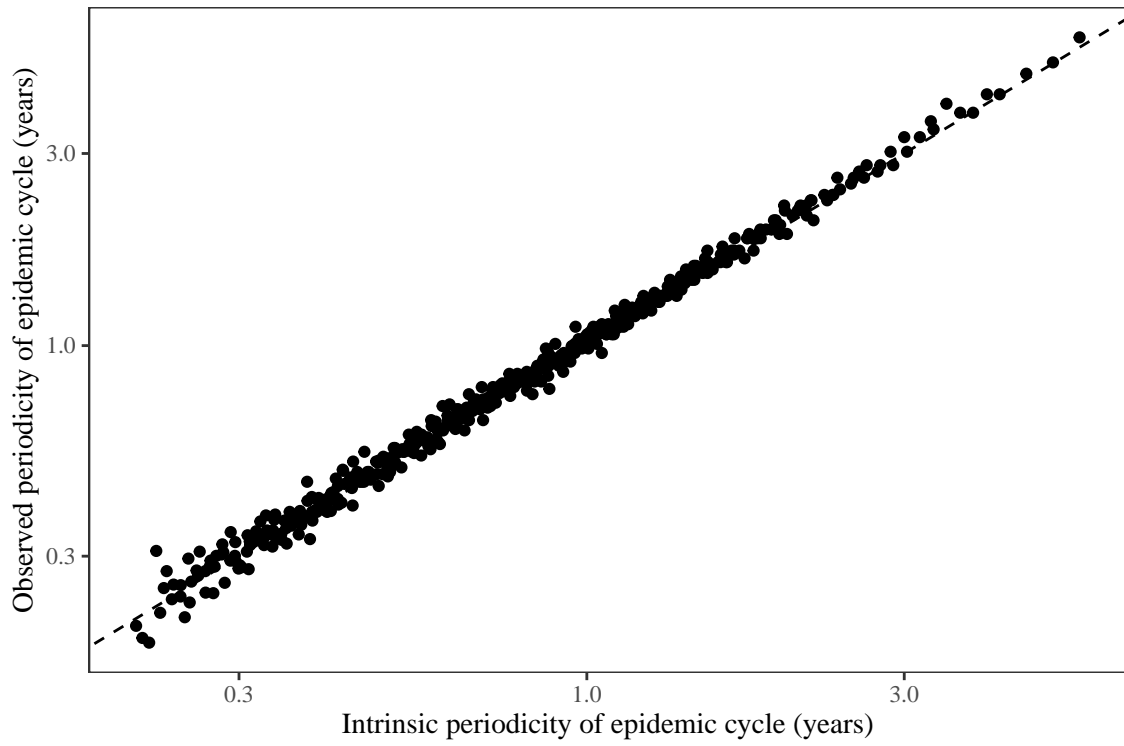


Figure S13: **Comparison between the observed and intrinsic periodicity of the epidemic cycle of the seasonally unforced SIRS model.** The observed periodicity of the epidemic corresponds to the periodicity at which maximum spectral density occurs. The intrinsic periodicity of the epidemic corresponds to  $2\pi/\text{Im}(\lambda)$ , where  $\text{Im}(\lambda)$  is the imaginary part of the eigenvalue.

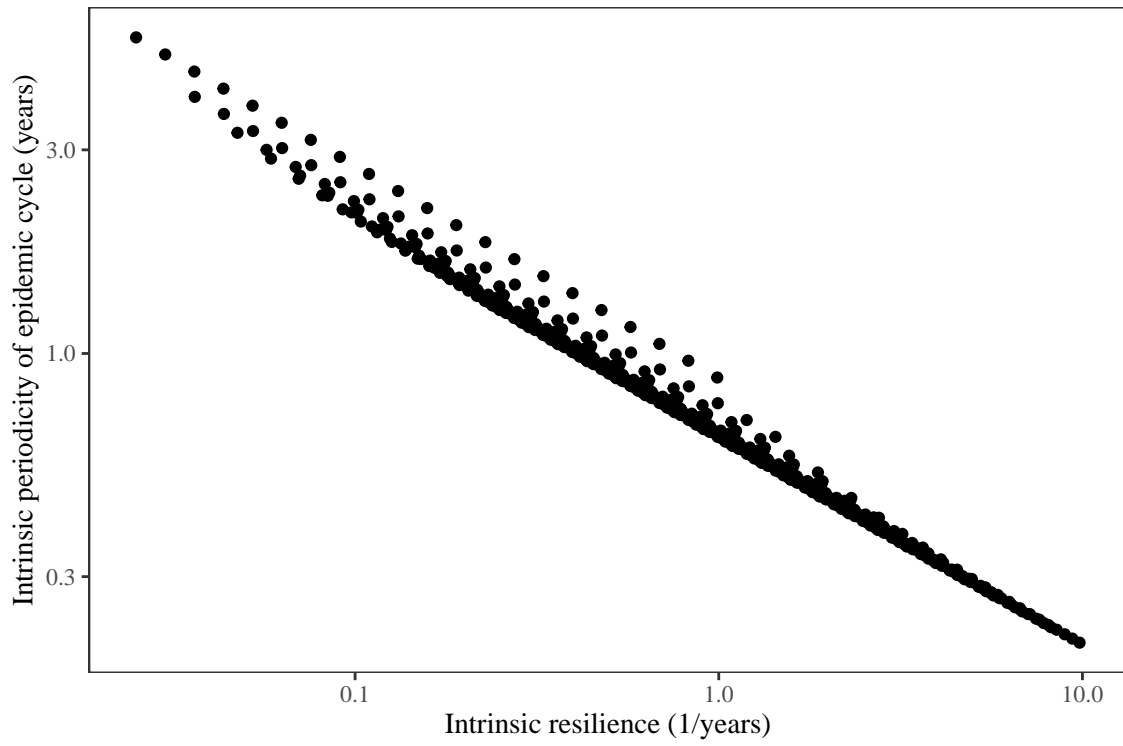
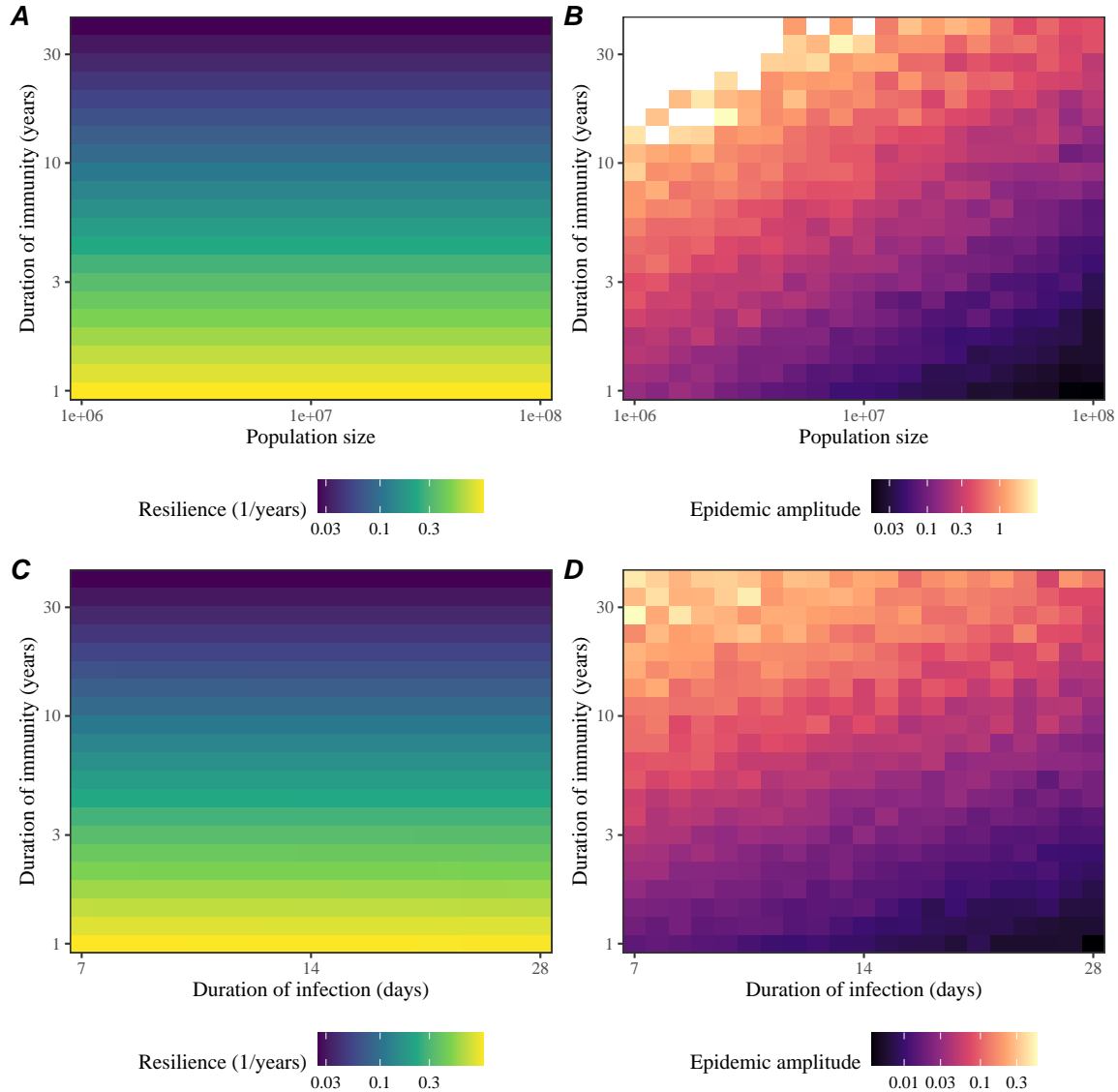
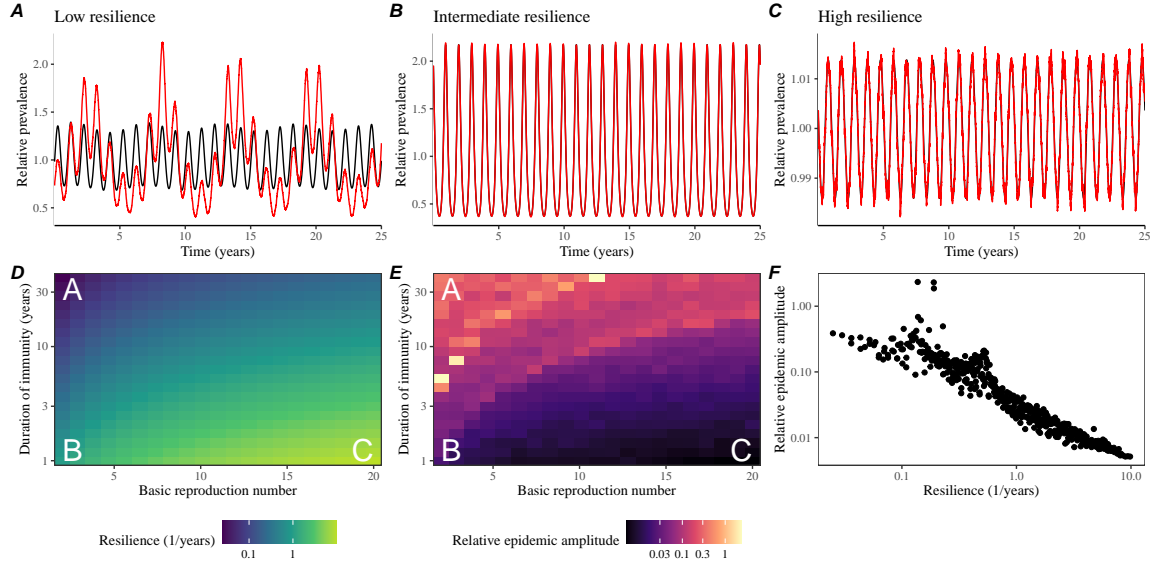


Figure S14: **Comparison between the intrinsic resilience and periodicity of the epidemic cycle of the seasonally unforced SIRS model.** The intrinsic resilience of the epidemic corresponds to the negative of the real value of the eigenvalue  $-\text{Re}(\lambda)$ . The intrinsic periodicity of the epidemic corresponds to  $2\pi/\text{Im}(\lambda)$ , where  $\text{Im}(\lambda)$  is the imaginary part of the eigenvalue.



**Figure S15: Impact of population size and the average duration of infection of a host-pathogen system on its sensitivity to stochastic perturbations.** (A) Intrinsic resilience of a system as a function of population size and the average duration of immunity. (B) Epidemic amplitude as a function of population size and the average duration of immunity. (C) Intrinsic resilience of a system as a function of the average duration of infection and immunity. (D) Epidemic amplitude as a function of the average duration of infection and immunity. The epidemic amplitude corresponds to  $(\max I - \min I)/(2\bar{I})$ , where  $\bar{I}$  represents the mean prevalence.



**Figure S16: Linking resilience of a host-pathogen system to its sensitivity to stochastic perturbations for the seasonally forced SIRS model.** (A–C) Epidemic trajectories of a stochastic SIRS model with demographic stochasticity across three different resilience values: low, intermediate, and high. The relative prevalence was calculated by dividing infection prevalence by its mean value. Black lines represent deterministic epidemic trajectories. Red lines represent stochastic epidemic trajectories. (D) The intrinsic resilience of the seasonally unforced system as a function of the basic reproduction number  $\mathcal{R}_0$  and the duration of immunity. (E) The relative epidemic amplitude, a measure of sensitivity to stochastic perturbations, as a function of the basic reproduction number  $\mathcal{R}_0$  and the duration of immunity. To calculate the relative epidemic amplitude, we first take the relative difference in infection prevalence between stochastic and deterministic trajectories:  $\epsilon = (I_{\text{stoch}} - I_{\text{det}})/I_{\text{det}}$ . Then, we calculate the difference between maximum and minimum of the relative difference and divide by half:  $(\max \epsilon - \min \epsilon)/2$ . Labels A–C in panels D and E correspond to scenarios shown in panels A–C. (F) The relationship between pathogen resilience and relative epidemic amplitude.

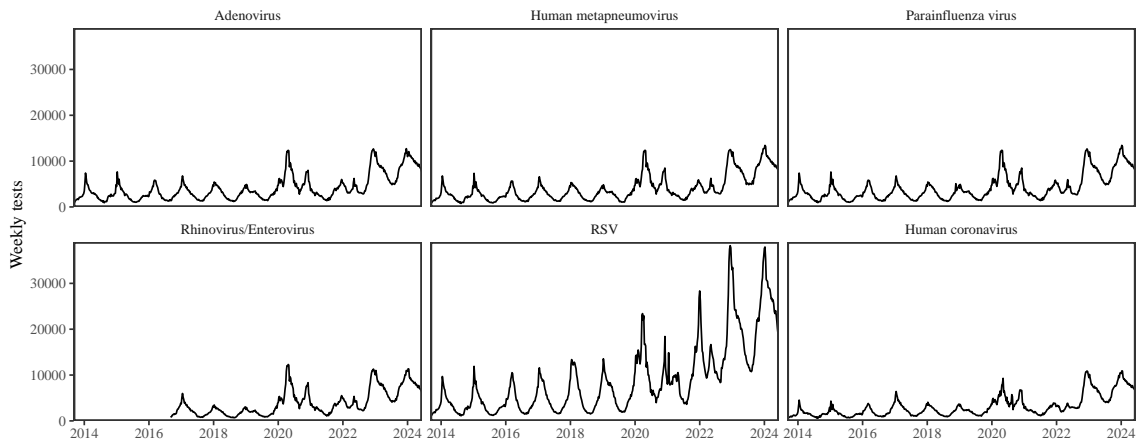


Figure S17: Testing patterns for respiratory pathogens in Canada.

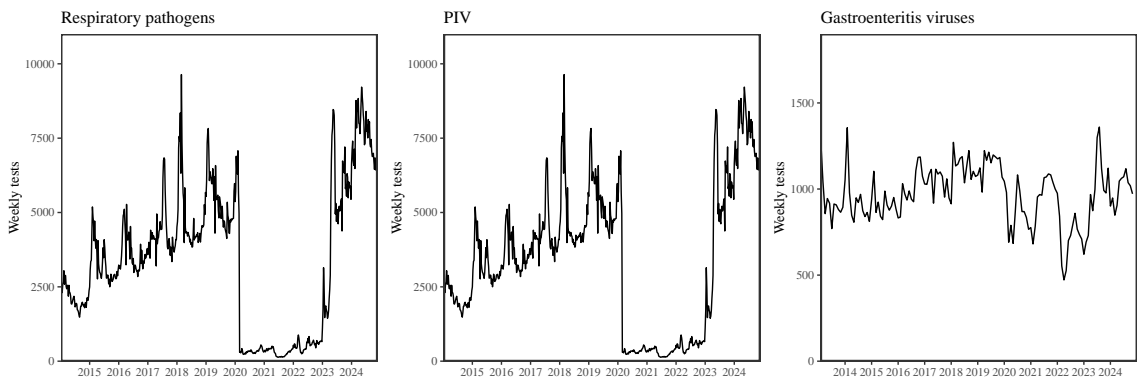


Figure S18: Testing patterns for respiratory pathogens, PIV, and gastroenteritis viruses in Hong Kong.

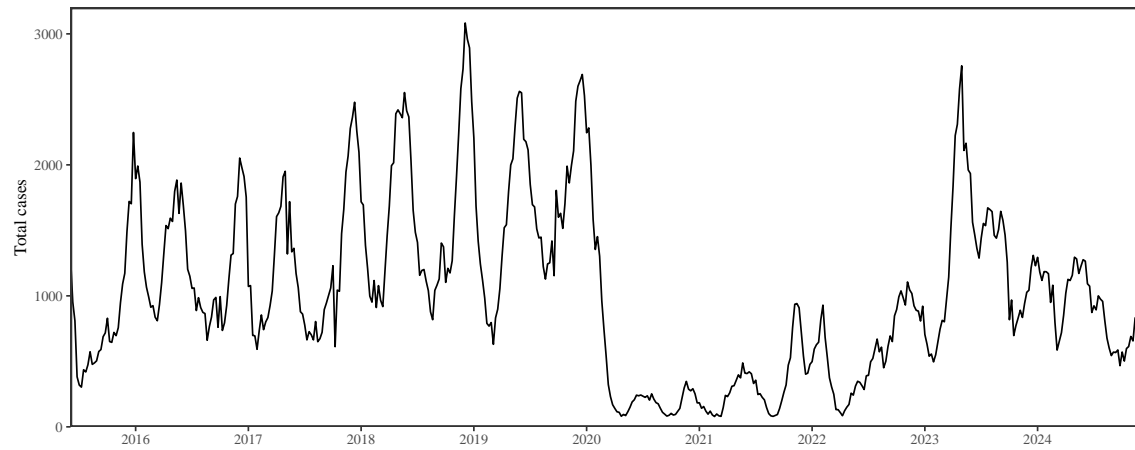


Figure S19: Total number of reported respiratory infection cases in Korea.

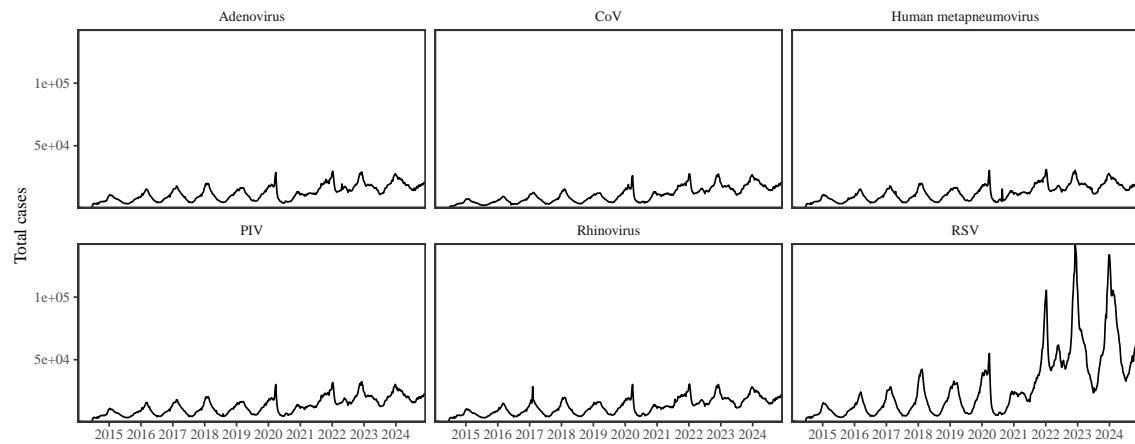


Figure S20: Testing patterns for respiratory pathogens in the US reported through the NREVSS.